The Astrophysical Journal, 973:148 (20pp), 2024 October 1 https://doi.org/10.3847/1538-4357/ad67d7

Dissipation of AGN Jets in a Clumpy Interstellar Medium

Riju Dutta[1], Prateek Sharma[1], Kartick C. Sarkar[2,3], and James M. Stone[4]
[1] Department of Physics, Indian Institute of Science, Bangalore 560012, India; rijudutta@iisc.ac.in, prateek@iisc.ac.in
[2] School of Physics and Astronomy, Tel Aviv University, Tel Aviv, 6997801, Israel
[3] Dept. of Space, Planetary & Astronomical Sciences and Engineering, Indian Institute of Technology Kanpur, India
[4] Institute for Advanced Study, 1 Einstein Drive, Princeton, NJ 08540, USA
Received 2023 December 31; revised 2024 July 20; accepted 2024 July 22; published 2024 September 27

Abstract

Accreting supermassive black holes frequently power jets that interact with the interstellar medium (ISM)/circumgalactic medium, regulating star formation in the galaxy. Highly supersonic jets launched by active galactic nuclei (AGN) power a cocoon that confines them and shocks the ambient medium. We build on the models of narrow conical jets interacting with a smooth ambient medium, including the effect of dense clouds, which are an essential ingredient of a multiphase ISM. The key physical ingredient of this model is that the clouds along the supersonic jet beam strongly decelerate the jet head but the subsonic cocoon easily moves around the clouds without much resistance. We propose scalings for important physical quantities—cocoon pressure, head and cocoon speed, and jet radius. For the first time, we obtain the analytic condition on the ambient medium's clumpiness for the jet to dissipate within the cocoon and verify it with numerical simulations of conical jets interacting with a uniform ISM with embedded spherical clouds. A jet is defined to be dissipated when the cocoon speed exceeds the speed of the jet head. We compare our models with more sophisticated numerical simulations and direct observations of jet–ISM interaction (e.g., quasar J1316+1753), and we discuss implications for the Fermi/eROSITA bubbles. Our work also motivates effective subgrid models for AGN jet feedback in a clumpy ISM unresolved by the present generation of cosmological galaxy formation simulations.

Unified Astronomy Thesaurus concepts: Galaxy jets (601); Interstellar medium (847); Interstellar clouds (834); Radio jets (1347)

1. Introduction

Jets—which transport energy over large distances in a small solid angle—are ubiquitous in astrophysics, from nonrelativistic protostellar jets (see, e.g., Bally 2016 for a review) to ultrarelativistic jets launched by stellar (e.g., Mirabel & Rodríguez 1998) and supermassive black holes (SMBHs; for a recent review, see Blandford et al. 2019). Jet launching appears to be commonly associated with the formation of an accretion disk. After being launched, the active galactic nucleus (AGN) jets interact with the ambient medium, which determines the observational appearance of objects such as radio galaxies (see Saikia 2022 for a recent observational review). Radio emission produced by relativistic electrons gyrating around magnetic fields and detected by our radio telescopes has allowed us to put together large catalogs of radio galaxies. These have historically revealed their two broad classes—the brighter FR II galaxies, with hot spots at the edge of the radio bubbles, and the dimmer FR I galaxies, which are brighter along the jet's path (Fanaroff & Riley 1974). Recent observations (e.g., Baldi et al. 2018; Sabater et al. 2019) show that most massive galaxies have dimmer radio emission at most times.

AGN jets not only are the signposts of SMBHs but also play an active role in regulating star formation and growth of SMBHs in their host halos (Alexander & Hickox 2012; Gaibler et al. 2012; Mandal et al. 2021). The mechanical energy dumped by these jets in the surrounding interstellar medium (ISM) and the diffuse intracluster medium (ICM)/circumgalactic medium (CGM) is enough to offset radiative cooling losses of these massive atmospheres (for a review, see Fabian 2012). One of the still-unresolved problems in this field is how narrow jets can effectively isotropically heat the ICM/CGM (see, e.g., McNamara & Nulsen 2007; Yang & Reynolds 2016; Meece et al. 2017; Martizzi et al. 2019; Choudhury & Reynolds 2022; Bourne & Yang 2023). To understand the AGN heating mechanism in these systems, we must understand the physics of the interaction of the jet and the ambient medium, the main subject of our paper.

The theoretical proposals to explain the broad classification of radio galaxies involve diverse processes (for a review, see Hardcastle & Croston 2020). For example, magnetic kink instability of the jet makes it unstable to helical perturbations and dissipates it along its path, producing an FR I–type appearance (e.g., Tchekhovskoy & Bromberg 2016). Other models include the interaction of the jet with a clumpy and stratified ISM (Sutherland & Bicknell 2007; Mukherjee et al. 2016, 2018). Simulations of jet–ISM interactions, focusing in particular on the efficiency of the transfer of the jet's energy and momentum to the clumpy medium, were presented by Wagner & Bicknell (2011) and Wagner et al. (2012, 2013).

This paper investigates the interaction of a collimated hydrodynamic AGN jet with a clumpy medium with analytic estimates and high-resolution 3D hydrodynamic simulations. In particular, we derive the physical condition on the clumpiness of the ISM for jet dissipation in a clumpy medium. The jet is dissipated when the jet head is confined within a roughly isotropic cocoon. Our scaling for jet dissipation can be applied in various contexts, from a physically motivated implementation of jet feedback in cosmological galaxy formation

simulations that can inject the appropriate amounts of thermal and kinetic feedback for a given resolution to explaining the appearance of radio galaxies.

An analytical model for jet head propagation and cocoon expansion as a function of time in a smooth medium was given by Bromberg et al. (2011). Their main conclusion is that collimated jets propagating in a uniform medium always give rise to narrow cocoons. This conclusion, however, would need to be modified in a clumpy medium with a large density contrast between the clouds and the low-density diffuse phase. In such a medium, where dense clouds obstruct the jet for a large fraction of the propagation time, the jet head encounters a relatively high effective density. On the other hand, the overpressured cocoon, whose internal velocities are much smaller than its sound speed, expands faster through the low-density diffuse phase that fills the space between the clouds. Hence, it encounters a much lower effective density.[5] This effect leads to much wider and isotropic cocoons than expected in a uniform medium. Therefore, the calculations of Bromberg et al. (2011) would need to be modified in two ways. First, instead of the ambient density ρ_H, we need two different effective ambient densities for head propagation and cocoon expansion. Second, the volume of the cocoon gas would need to be multiplied by a factor of $1 - f_V$, where f_V is the volume filling factor of the dense clouds inside the cocoon.

The above considerations allow us to formulate, for the first time, a criterion for a jet to be dissipated in a clumpy medium. We present analytical estimates of the dissipation criteria for a simple two-phase medium where dense clouds are distributed uniformly. We find that the dissipation criterion only depends on the volume filling factor and the density contrast of the clouds. We verify our analytical estimates using high-resolution numerical simulations and find that the analytical criterion for dissipation works well, except that we need to calibrate the cocoon size with numerical simulations. Therefore, our dissipation criterion can be used in a wide range of systems to understand jet–ISM interaction and even provide predictions for the system's evolution.

In Section 2, we present our jet–ISM interaction model's physical and numerical setup. Section 3 presents analytic estimates for key physical quantities (e.g., cocoon pressure, head/cocoon speed) in different jet–ISM interaction scenarios and the jet dissipation criterion. Section 4 tests the analytic models with appropriately designed hydrodynamic simulations. Section 5 discusses the broad astrophysical implications of our work, and Section 6 summarizes our paper.

2. Setup

The ISM around the AGN jets can be very complex in geometry and temperature/density distribution (see Heywood et al. 2022 and references therein). Therefore, we consider the simplest model of a clumpy medium—a uniform medium with homogeneous density in which overdense spherical clouds of radius $R_{\rm cl}$ are spread randomly in pressure equilibrium with the intracloud medium. This oversimplification makes the setup somewhat analytically tractable. Insights gained from this simple model can be extended to a more realistic situation.

[5] The qualitative difference between the clouds interacting with the jet and the clouds interacting with the cocoon is shown in the following video of an equivalent shallow water setup: http://youtu.be/DUpSwMMrGfk.

Table 1
The Jet and Homogeneous ISM Parameters Used in Most Simulations

θ_0	L_j (erg s^{-1})	v_j	ρ_H (m_p cm^{-3})	T_H (K)	$L_{\rm box}$ (kpc)
10°	1.1×10^{42}	0.05 c	1	10^4	0.8
					0.4

Note. Cubical boxes with sides 0.4 and 0.8 kpc are used for different simulations listed in Tables 2 and 3.

2.1. Physical Setup

First, we generalize the analytic model of Bromberg et al. (2011) for the structure of the cocoon driven by narrow AGN jets in a uniform medium to the nonrelativistic jet regime (Section 3.1) and calibrate it with numerical simulations (Section 4.1). Next, we treat the impact of clouds on jet and cocoon evolution both analytically (Section 3.3) and with numerical simulations (Section 4.2).

The clumpy medium that we consider consists of a volume filling warm phase with a constant density $\rho_H = 1 m_p$ cm^{-3} and temperature 10^4 K (mimicking the warm/ionized diffuse phase of the ISM), within which uniformly distributed spherical dense clouds are positioned randomly. The clouds' density and volume filling fraction are denoted by $\rho_{\rm cl}$ and f_V, respectively. The clouds are in pressure equilibrium with the diffuse warm phase and have a fiducial radius of 5 pc.

We inject a conical jet with a half-opening angle (θ_0) of 10° into this medium. The radius of the jet at its injection height is 2 pc, which is small compared to the collimated radius of the jet $R_j \sim$ 10–20 pc (see Equation (19d) and Figure 2) for our runs. The total power of the jet (L_j) is 1.1×10^{42} erg s^{-1}, which is dominated by its kinetic energy (the ratio of thermal and kinetic energy densities is 10% at the injection point). The initial jet velocity (v_j) is assumed to be 1.5×10^4 km s^{-1} ($c/20$, where c is the speed of light), which is highly supersonic compared to the ambient medium with a sound speed $\approx$10 km s^{-1}. Thus, the jets are also overpressured with respect to the ambient medium at the injection point, by a factor of $\approx 10^5$ (see middle panel of Figure 2). Table 1 lists our parameter values for a quick reference.

For all runs in this work, the parameters governing the jet injection (θ_0, L_j, and v_j) are fixed at the values above. We vary the parameters describing the ambient medium—the cloud size ($R_{\rm cl}$), cloud density ($\rho_{\rm cl}$), and volume fraction of clouds (f_V). However, our analytic scaling relations allow us to apply our findings to a general choice of parameters.

2.2. Numerical Setup

For our hydrodynamic simulations, we use the AthenaK code (Stone et al. 2020; Stone et al., in preparation) with a Harten–Lax–van Leer–Einfeldt (HLLE) Riemann solver, RK2 time integration, and piecewise linear reconstruction. The code solves the following fluid equations in their conservative form:

$$\frac{\partial \rho}{\partial t} + \nabla \cdot (\rho \boldsymbol{v}) = 0, \tag{1a}$$

$$\frac{\partial (\rho \boldsymbol{v})}{\partial t} + \nabla \cdot (\rho \boldsymbol{v} \otimes \boldsymbol{v}) + \nabla P = 0, \tag{1b}$$

$$\frac{\partial E}{\partial t} + \nabla \cdot ((E + P)\boldsymbol{v}) = 0, \tag{1c}$$

Table 2
List of Simulations Where the Cloud Density Is Held Constant at $100m_p$ cm^{-3} and f_V and R_{cl} Are Varied

Label	R_{cl} (pc)	f_V	v_h (10^3 km s^{-1})	v_c (10^3 km s^{-1})	f_L
uniform	0	0.0	0.99	0.33	0.0
f0006R5	5	0.00625	0.64	0.33	0.08
f0012R5	5	0.0125	0.57	0.33	0.11
f0025R5	5	0.025	0.45	0.32	0.19
f005R5	5	0.05	0.41	0.30	0.22
f0075R5	5	0.075	0.39	0.29	0.24
f01R5	5	0.1	0.36	0.28	0.28
f0012R6.3	6.3	0.0125	0.50	0.33	0.15
f0025R6.3	6.3	0.025	0.44	0.33	0.20
f0025R7.9	7.9	0.025	0.43	0.33	0.21
f005R7.9	7.9	0.05	0.43	0.34	0.21
f01R10	10	0.1	0.29	0.34	0.41

Note. The simulation name f*xx*R*y* indicates a volume filling fraction, $f_V = x.xx$, and a cloud radius, $R_{cl} = y$ pc. For these runs, the simulation box is a cube of side 0.8 kpc, with the highest resolution on the jet axis being 0.4 pc. Velocities are averaged until the jet material is still in the box.

$$E = \frac{\rho \boldsymbol{v} \cdot \boldsymbol{v}}{2} + \frac{P}{\gamma - 1}. \tag{1d}$$

Here ρ is the mass density, P is the thermal pressure, $\boldsymbol{v}$ is the velocity of the gas at any given point in space and time, and γ is the adiabatic index of the ideal gas. We do not include gravity (neither external nor self-gravity) since it affects the dynamics on larger timescales/length scales than studied here. We also ignore radiative cooling for the current work to focus on the hydrodynamic interactions. We discuss the effect of neglecting radiative cooling in Section 5.2.

2.2.1. Grid and Boundary Conditions

The simulation domain is taken to be a cubical box of side $L_{box} = 0.8$ and 0.4 kpc for two sets of runs listed in Tables 2 and 3, respectively. The outer regions have a base resolution of 512 cells along each side (i.e., 1.28 cells pc^{-1} for $L_{box} =$ 0.4 kpc, and half this value for the larger boxes). In the inner regions close to the jet's axis (z-axis), we employ static mesh refinement (SMR). Due to the SMR, the region defined by $|x| < 25$ pc and $|y| < 25$ pc ($|x| < 50$ pc and $|y| < 50$ pc for $L_{box} = 0.8$ kpc) has a 4 × higher resolution (of 5.12 cells pc^{-1} for $L_{box} = 0.4$ kpc and 2.56 cells pc^{-1} for $L_{box} = 0.8$ kpc). Thus, the clouds in the path of the jet have nearly 50 (25) cells across their diameter for $R_{cl} = 5$ pc and $L_{box} = 0.4$ (0.8) kpc. This ensures that the jet collimation shock and jet–cloud interactions are sufficiently resolved. We run each simulation until the cocoon or the jet head moves out of the computational domain. For the larger box simulations, with $L_{box} = 0.8$ kpc, the same mesh pattern is used such that the resolution everywhere is smaller by 2.

The jet is injected at the bottom boundary inside a half-opening angle of θ_0 relative to the $+z$-direction, with the velocity pointing radially outward, within a jet injection radius of 2 pc (same for both $L_{box} = 0.8$ and 0.4 runs).[6] At the lower z-boundary corresponding to the base of the jet, we impose outflow boundary conditions (zero gradients) inside the injection radius of 2 pc and reflective boundary conditions outside it. At all the other boundaries, we impose outflow boundary conditions. The reflective boundary condition at the bottom boundary outside the jet injection region mimics the interaction of the cocoon with its counterpart in the $-z$ domain. We run our simulations until the cocoon outer shock reaches the lateral edges of the box or the jet head reaches the upper z-boundary. We restrict all our measurements within this time.

Table 3
List of Simulations Where the Pattern of Clouds Is Held Constant at $R_{cl} = 5$ pc, $f_V = 0.1$ and Cloud Density (ρ_{cl}) Is Varied

Label	ρ_{cl} (m_p cm^{-3})	v_h (10^3 km s^{-1})	v_c (10^3 km s^{-1})	Dissipated
f01d12	12	1.00	0.42	No
f01d25	25	0.74	0.42	No
f01d50	50	0.65	0.41	No
f01d75	75	0.42	0.34	Marginally
f01d100	100	0.16	0.36	Yes

Note. For these runs, the simulation box is a cube of side 0.4 kpc, and the highest resolution is 0.2 pc. Velocities are averaged over the time when the jet has collimated, and jet material is still in the box. Unlike for constant ρ_{cl} runs in Table 2, we do not hollow out a region near the center for these runs.

2.2.2. Cloud Distribution

To carefully compare our simulations with analytic models, we run two kinds of simulations: ones with a fixed density but different cloud patterns (i.e., changing the initial volume filling fraction and cloud radius, as listed in Table 2), and ones with different densities for a fixed cloud pattern (listed in Table 3). For the former, we hollow out a small cuboidal volume close to the center, of horizontal width 14 pc and height 85 pc, where we do not place any clouds (see small green rectangles in panels of Figure 1). This allows the collimation shock to form without interruption, which gives us enough time to measure the cocoon and head properties before they leave the box. Such hollowing out does not affect the later evolution of jets after the formation of the collimation shock but allows us to compare simulations with analytic scalings unambiguously. The runs with different cloud density do not impose this hollowing out.

The specific location of clouds can affect the jet head and cocoon properties at certain times. Since the jet head only samples a small fraction of the box volume and interacts with ≈10–20 clouds, their numbers and positions relative to the jet axis can be subject to statistical fluctuations, which in turn can lead to differing head velocities. To avoid statistical fluctuations and to measure trends with cloud properties, we place the clouds at identical locations and remove a specified random fraction of them as we decrease the volume fraction or

[6] This means that the jet injection radius is resolved only by ≈5 grid cells for $L_{box} = 0.8$ kpc, and the injected jet power can be off from the value mentioned in Table 1. This is tolerable since the jet dissipation criterion depends only on the jet angle θ_0 and the clumpiness (see Equation (27)), and not on jet power.

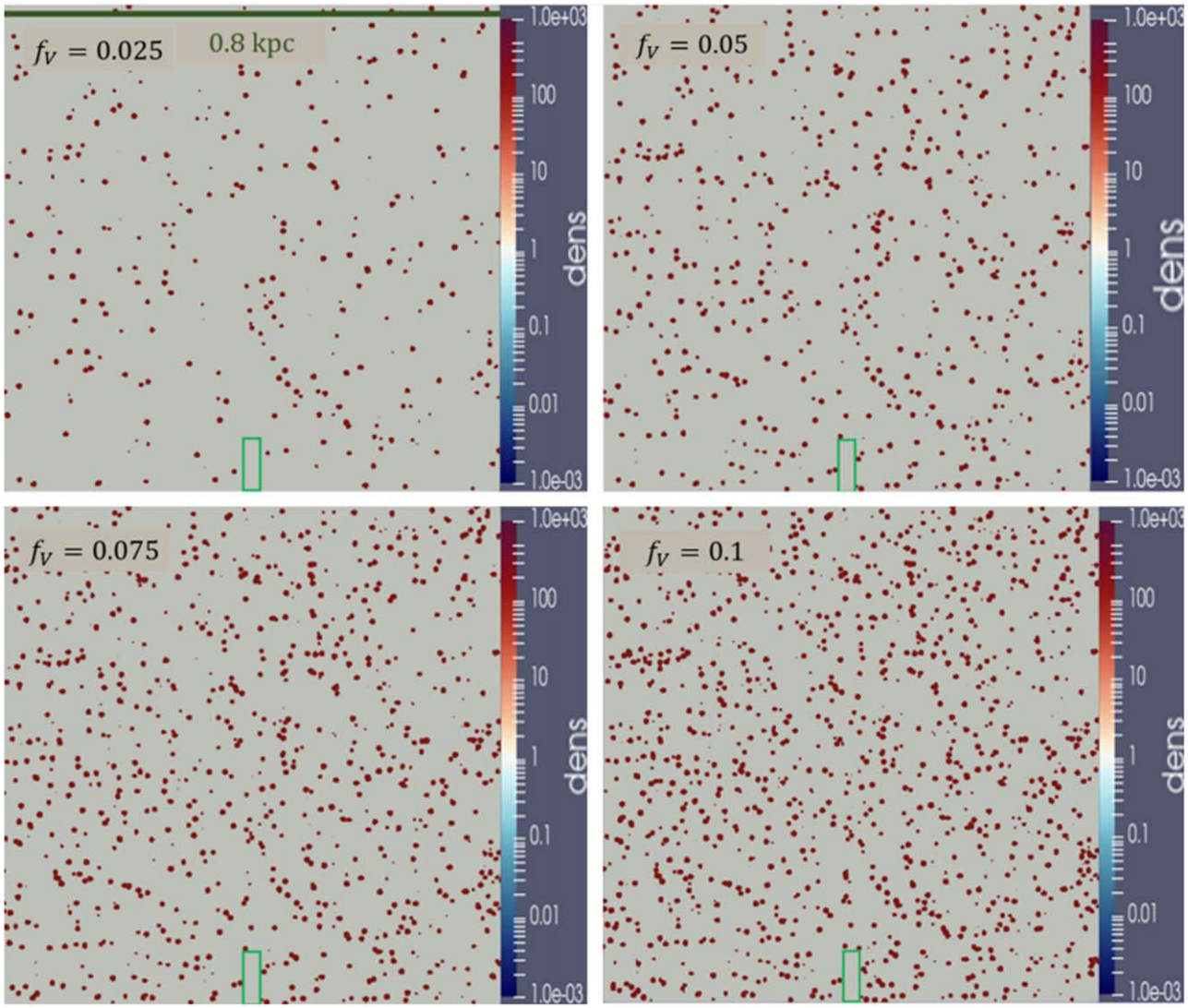

Figure 1. Snapshots of density (in units of $m_p\,\mathrm{cm}^{-3}$) in the y-z plane for $L_{\mathrm{box}} = 0.8$ kpc simulations with the same cloud pattern (Table 2) but a varying volume fraction of $f_V = 0.1$, 0.075, 0.05, and 0.025. The cloud density ρ_{cl} is $100 m_p\,\mathrm{cm}^{-3}$, and cloud size is $R_{\mathrm{cl}} = 5$ pc. We maintain the same cloud locations for comparison with analytic scalings but remove some clouds across these runs (see Section 2.2.2). Also note that for faster collimation of the conical jet we hollow out a small cuboidal volume region close to the center (shown in green) that does not contain any clouds.

increase the cloud radius for a fixed volume fraction (f_V; see Figure 1 for an example). Cloud locations are the same for the runs within Tables 2 and 3, but not across them.

2.2.3. Measuring Jet Head and Cocoon Positions

At time steps separated by 0.02 Myr, we analyze 2D slices of the box in the y-z plane ($x = 0$). From these slices, we extract the lateral size of the cocoon (r_c) and the height of the jet head (z_h). We calculate r_c as the average of the maximum lateral extent of the cocoon in the $+y$ and $-y$ directions (the two values are quite similar in a medium where the cloud distribution is statistically homogeneous and isotropic on the scale of the cocoon). We measure z_h to be the length of the high-velocity ($v_z > 10^4\,\mathrm{km\,s}^{-1}$) jet. Sometimes a cloud can obstruct the jet without a clear jet head. In such cases, we assume the cloud location to be the z_h. The scales r_c and z_h are measured after the jet collimates but before any cocoon material leaves the box.

3. Analytic Estimates

Before moving on to 3D hydrodynamic simulations of jet–ISM interaction, we provide some analytic estimates. We start with a recapitulation of the analytic model of jet collimation in a homogeneous medium from Bromberg et al. (2011) and generalize it to nonrelativistic jets (Section 3.1). We generalize these estimates to a clumpy medium in Section 3.3.

3.1. Collimated Jet in a Uniform Medium

Even the earliest works on AGN jets recognized the anisotropy of an AGN jet expanding into a uniform medium (e.g., Blandford & Rees 1974; Scheuer 1974). Later works (e.g., Begelman & Cioffi 1989; Matzner 2003) calculated the velocity of the head pushed by the jet ram pressure and the cocoon velocity driven by the cocoon pressure, but the width of the collimated jet was not calculated self-consistently. Building on the earlier works on the structure of jet collimation shock (e.g., Komissarov & Falle 1997), Bromberg et al. (2011)

presented a model for the structure of the cocoon blown by jets interacting with a smooth medium.

We assume a steady cold jet with power L_j, jet velocity v_j, and jet injection angle θ_0. These three parameters define all the jet properties. The cold ambient medium is assumed to have a uniform density ρ_H.[7] The jet head speed is v_h, the cocoon expansion speed is v_c, and the cocoon pressure is P_c. Although the calculations presented here are for a nonrelativistic jet, the scaling relations derived should apply to mildly relativistic jets and qualitatively to even relativistic jets.

For a collimated jet propagation into an ambient medium, the jet terminates (or creates a reverse shock) just behind the forward shock (see Figure 3 of Sarkar et al. 2023 for a qualitative depiction). Therefore, we can apply momentum flux conservation along the jet direction, which in the forward shock frame is

$$\rho_j(v_j - v_h)^2 + P_j = \rho_H v_h^2 + P_a, \tag{2}$$

where P_j and P_a are the pressures in the jet and ambient medium, respectively, and ρ_j is the jet density just upstream of the head. The jet density, ρ_j, and velocity, v_j, are roughly constant between the collimation shock and the jet head since the jet quickly becomes cylindrical after the collimation shock. Now, assuming a strong forward shock and a kinetic-energy-dominated jet, the pressures can be neglected, leading to

$$v_h = \frac{v_j}{1 + \sqrt{\frac{\rho_H}{\rho_j}}} \approx \sqrt{\frac{\rho_j}{\rho_H}} v_j, \tag{3}$$

where in the last equality we assume that $\rho_j \ll \rho_H$. Such an assumption is appropriate for the AGN jets, which generally have low density. One needs to relax this assumption in cases where the jets may have higher density, such as proto-stellar jets.

For the cocoon expansion (perpendicular to the jet direction), we again consider momentum flux conservation in the frame of the horizontal forward shock. Assuming a strong shock, we get

$$\frac{1}{4}\rho_H v_c^2 + P_c = \rho_H v_c^2, \tag{4}$$

so that

$$v_c = \sqrt{\frac{4}{3}\frac{P_c}{\rho_H}}. \tag{5}$$

In the second step, using these expressions obtained for v_h and v_c and assuming a cylindrical geometry for the entire cocoon, we get the following estimate for the volume of the cocoon:

$$V_c \approx \pi v_c^2 v_h t^3, \tag{6}$$

where t is time. Therefore, the pressure within the cocoon $P_c \approx (2/3)L_j t/V_c$. Now, combining with Equation (5), we obtain the expression for the cocoon pressure:

$$P_c = \sqrt{\frac{L_j \rho_H}{2\pi v_h t^2}}. \tag{7}$$

[7] Our results, for both smooth and clumpy ISM, can be easily generalized to a power-law profile of the ambient medium following Bromberg et al. (2011).

The key advance in Bromberg et al. (2011) was to include the expression for the jet radius, R_j, by solving for the structure of the jet collimation shock. The collimation shock turns an initially conical jet into a cylindrical one after a certain height, $H_t/2$, and the jet speed and density are roughly constant along the cylindrical jet beam. Following Bromberg et al. (2011) and generalizing their calculation to a nonrelativistic jet (see their Equation (9)), the height of the tip of the collimation shock is given as

$$H_t = \sqrt{\frac{2L_j}{\pi v_j P_c}}, \tag{8}$$

such that the jet radius is $R_j = \theta_0 H_t/2$. Therefore, the cross-section area of the jet head, Σ_j, is given by

$$\Sigma_j \equiv \pi R_j^2 = \frac{L_j \theta_0^2}{2P_c v_j}. \tag{9}$$

The jet pressure outside the collimation shock equals the cocoon pressure. The jet density in the collimated cylindrical jet (with a roughly constant radius R_j) equals (using Equation (9) and expressing jet luminosity in terms of its density, $L_j = 0.5\rho_j v_j^3 \pi R_j^2$)

$$\rho_j \approx \frac{4P_c}{v_j^2 \theta_0^2}. \tag{10}$$

Combining Equations (10), (7), and (3), we obtain

$$v_h \approx 2\left(\frac{L_j}{4\pi\theta_0^4 \rho_H t^2}\right)^{1/5} \approx 2.8 \times 10^3 \text{ km s}^{-1}\left(\frac{L_{j,42}}{\theta_{0,10}^4 \rho_{H,m_p} t_{\rm Myr}^2}\right)^{1/5} \tag{11a}$$

$$v_c \approx \sqrt{\frac{4}{3}}\left(\frac{\theta_0 L_j}{4\pi\rho_H t^2}\right)^{1/5} \approx 2.8 \times 10^2 \text{ km s}^{-1}\left(\frac{\theta_{0,10} L_{j,42}}{\rho_{H,m_p} t_{\rm Myr}^2}\right)^{1/5} \tag{11b}$$

$$P_c \approx \left(\frac{\theta_0^2 L_j^2 \rho_H^3}{16\pi^2 t^4}\right)^{1/5} \approx 9.8 \times 10^{-10} \text{ dyn cm}^{-2}\left(\frac{\theta_{0,10}^2 L_{j,42}^2 \rho_{H,m_p}^3}{t_{\rm Myr}^4}\right)^{1/5}, \tag{11c}$$

where $L_{j,42} = L_j/(10^{42} \text{ erg s}^{-1})$, $\theta_{0,10} = \theta_0/10°$, $\rho_{H,m_p} = \rho_H/m_p$, and $t_{\rm Myr} = t/\text{Myr}$. Note that the cocoon and head properties only depend on the usual combination of L_j, ρ_H, and t as in the standard wind-bubble solution (Weaver et al. 1977) but with an additional dependence on θ_0 such that

$$\frac{v_c}{v_h} \approx \frac{\theta_{0,10}}{10}. \tag{12}$$

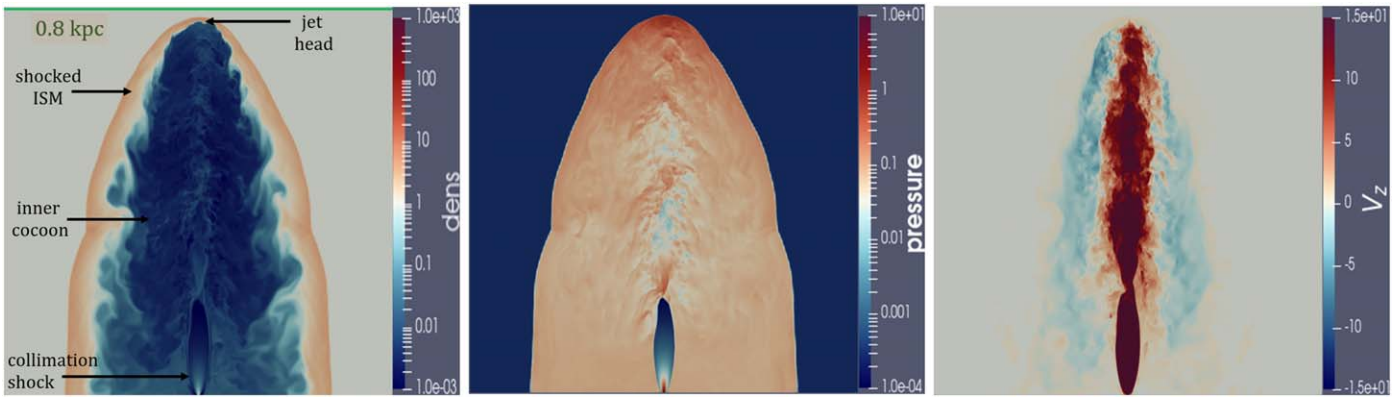

Figure 2. Snapshots in the y-z plane of density (m_p cm^{-3}; left), pressure (1.67×10^{-8} dyn cm^{-2}; middle), and vertical velocity (1000 km s^{-1}; right) for a jet in a uniform medium with $\rho_H = 1 m_p$ cm^{-3}, at time $t = 0.6$ Myr. Note the presence of the converging collimation shock driven by the overpressured cocoon, as described in Bromberg et al. (2011). This brings the jet into pressure equilibrium with the cocoon downstream of the convergence point. The shocked ISM is compressed in a dense shell that shows signs of shear instabilities at the inner boundary, pressure is almost constant throughout the cocoon, and there are backflows in the inner cocoon deflected from the jet head.

Now, from Equation (9), we find that the collimated jet radius evolves as

$$R_j \approx \left(\frac{\theta_0^8 L_j^3 t^4}{2\pi^3 v_j^5 \rho_H^3}\right)^{1/10} \approx 4.16 \text{ pc} \left(\frac{v_j}{c}\right)^{-1/2} \left(\frac{\theta_{0,10}^8 L_{j,42}^3 t_{\rm Myr}^4}{\rho_{H,m_p}^3}\right)^{1/10}, \quad (13)$$

which depends also on the jet velocity, unlike the head/cocoon parameters (Equations (11a)–(11c)). Equation (13) shows that even for a jet speed $v_j \approx 0.01c$ the self-consistently collimated jet radius is roughly tens of parsecs. Thus, resolving the collimation shock is impossible for large-scale galaxy formation simulations, and hence the jets must be included as a subgrid model (see Section 5.4). Our jets are underdense relative to the ambient medium, with the jet density to the ambient medium density given by (combining Equations (11c) and (10))

$$\frac{\rho_j}{\rho_H} \approx \left(\frac{8 L_j}{\pi \theta_0^4 \rho_H v_j^5 t^2}\right)^{2/5} \approx 8.6 \times 10^{-5} \left(\frac{v_j}{c}\right)^{-2} \left(\frac{L_{j,42}}{\theta_{0,10}^4 \rho_{H,m_p} t_{\rm Myr}^2}\right)^{2/5}, \quad (14)$$

which for our $v_j/c = 0.05$ gives $\rho_j/\rho_H \approx 0.034$ (see left panel of Figure 2).

The analytic estimates above show that the jet+cocoon evolution is qualitatively different from the evolution of a spherical wind-blown bubble. As with the wind, the cocoon properties (v_h, v_c, P_c) depend on the appropriate dimensional combinations of L_j, ρ_H, and t, but there is also a dependence on another dimensionless parameter, the jet opening angle θ_0. The dependence on θ_0 comes not from dimensional arguments but from physical considerations. The height of the collimation shock (H_t) and the jet radius (R_j; see Equation (13)) depend on the jet velocity, similar to the termination shock radius for a spherical wind, which also depends on the ejecta velocity (e.g., Equation (9) in Sharma et al. 2014).

One of the key predictions of this jet–cocoon model is that for a collimated jet the aspect ratio of the cocoon, which can be approximated by v_c/v_h, is of the order of θ_0. This implies that such jets always produce narrow cocoons and hence are not dissipated in a smooth medium. Figure 2 shows the jet and cocoon structure for a jet expanding into a uniform medium. This model predicts a cocoon aspect ratio independent of the jet velocity/density. In contrast, previous simulations have reported a dependence on these quantities, possibly because they violate the conditions for self-similar evolution.[8] English et al. (2016), Weinberger et al. (2017), Huško & Lacey (2023), and Weinberger et al. (2023) explained such dependencies as being due to the varying momentum flux of the jet and strong backflows. However, most of these simulations considered only cylindrical jets and did not account for the self-collimation process of an initial conical jet. One needs further investigations to assess the conditions for which the shape of the cocoon is truly dependent on the jet velocity or density in a self-collimated jet.

3.2. Interaction of a Jet/Cocoon with Single/Few Clouds

Before studying the interaction of a jet with numerous clouds, it is useful to estimate some timescales for the interaction of a jet with a single cloud. The problem of the interaction of a supersonic uniform wind with a dense/cold cloud (the cloud-crushing problem), which applies to the jet–cloud interaction problem for $R_{\rm cl} \ll R_j$, has been studied exhaustively (Klein et al. 1994), but quantitative understanding is still lacking (Ranjan et al. 2011). The key conclusion from nonradiative simulations is that the cloud is shredded by compression and hydrodynamic (Kelvin–Helmholtz, Rayleigh–Taylor, and Richtmyer–Meshkov) instabilities over a few cloud-crushing times ($t_{\rm cc} = \sqrt{\rho_{\rm cl}/\rho_w} R_{\rm cl}/v_w$, where ρ_w is the wind density and v_w is the wind speed), much faster than it can become comoving over a drag timescale ($t_{\rm drag} = [\rho_{\rm cl}/\rho_w] R_{\rm cl}/v_w$).[9]

[8] Self-similar evolution is realized only for large Mach number shocks, light steady jets, and a power-law ambient medium.

[9] However, see Goldsmith & Pittard (2018) and Forbes & Lin (2019), who find a momentum exchange time of $\sim t_{\rm cc}$. This is understandable since the density contrast disappears after the cloud is mixed, and the cloud becomes comoving immediately after this.

A smaller number of works, mostly in the context of dense protostellar jets, have studied the interaction of jets narrower than or comparable to the cloud size (e.g., Raga & Canto 1996; de Gouveia Dal Pino 1999; Wang et al. 2000). These works show that the off-centered jets are deflected for some time before they clear out the cloud material from their path. For $R_j < R_{\rm cl}$, a jet impacting close to the center launches a shock into the cloud, and the jet head moves slowly through the cloud at a head velocity $v_h \approx \sqrt{\rho_j/\rho_{\rm cl}}\, v_j$ (analogous to Equation (3)). Thus, after $\approx 2R_{\rm cl}/v_h = 2t_{\rm cc}$, the jet is expected to drill through the cloud, leaving behind the cloud material, which is pushed laterally by the cocoon. In this case, too, the drag time is $t_{\rm drag} = (\rho_{\rm cl}/\rho_w)R_{\rm cl}/v_w$, longer than $t_{\rm cc}$. But in contrast to a cloud smaller than the jet beam, in this case the jet head can drill through the cloud, leaving behind most of the cloud mass that is not comoving with the jet head.

With multiple clouds interacting with the jet, collective effects can become important, and cloud destruction can be significantly delayed (e.g., Forbes & Lin 2019). Similarly, the destruction timescale can have a nontrivial dependence on $R_{\rm cl}/R_j$ for cloud size comparable to the jet radius. Irrespective of these complications, which are difficult to treat from first principles, in all cases the cloud material along the jet beam interacts strongly with the jet, but the cocoon essentially moves around the dense clouds. The clouds facing the jet beam are ablated and/or moved away from its path. In contrast, the clouds engulfed by the cocoon only encounter the shock for a short time ($\sim R_{\rm cl}/v_c$), after which they are embedded in the subsonic, low-density cocoon, which moves through the diffuse phase, avoiding the clouds. These concepts from jet–single/few cloud interaction motivate the timescale estimate presented in Section 3.3.3 for the interaction of a jet with uniformly distributed clouds.

3.3. Collimated Jet in a Clumpy Medium

It is useful to generalize the results from Section 3.1 to a more realistic setting of a clumpy ISM. A cloud present in the jet beam encounters a supersonic flow (jet velocity $\gg$ jet sound speed), leading to the formation of a strong bow shock with a bow wave angle $\sim \sin^{-1}(1/M_j)$, where $M_j = v_j/c_{s,j}$ is the jet Mach number. The bow shock persists until the cloud is fully ablated. On the other hand, the clouds inside the cocoon only face a subsonic flow and therefore do not create bow shocks. The subsonic cocoon material simply flows around the dense cloud. Thus, in a clumpy ISM with a small volume filling fraction of clouds, the supersonic jet would, on average, encounter material with an effective density, $\rho_{\rm eff}$, that is higher than the density of the homogeneous warm phase, ρ_H. Meanwhile, the overpressured subsonic cocoon can expand through the warm phase much faster, such that the relevant ambient density for cocoon expansion is ρ_H (similar to the propagation of a supernova blast wave in a clumpy ISM; e.g., McKee & Ostriker 1977). This leads to a head velocity lower than in a uniform medium of density ρ_H, leading to a smaller v_h/v_c. Now, if too many dense clouds are along the jet path, the average v_h/v_c will be smaller. At a critical number density of the clouds (or a critical value of $\rho_{\rm eff}$), the ratio can even become less than 1. After this point, the pressure-driven cocoon overtakes the ram-pressure-driven jet head even in the direction of the jet, and the whole cocoon expands in a near-spherical fashion. The jet is then said to be dissipated since the dynamics of the cocoon are no longer driven by the kinetic energy of the jet.

To model jet interaction with a clumpy medium, we begin by defining an effective density contrast, λ, as

$$\lambda \equiv \frac{\rho_{\rm eff}}{\rho_H}, \tag{15}$$

where $\rho_{\rm eff}$ (to be specified later) is the effective density encountered by the jet head. As we will see later, this effective density is a function of the cloud size, the volume filling fraction of the clouds (f_V), and the cloud density $\rho_{\rm cl}$. The new expressions for v_h and v_c (which replace Equations (3) and (5)) would therefore be

$$v_h = \sqrt{\frac{\rho_j}{\rho_{\rm eff}}}\, v_j, \tag{16}$$

$$v_c = \sqrt{\frac{4}{3}\frac{P_c}{\rho_H}}. \tag{17}$$

Now, in this model, Equation (6) for the volume of the cocoon would also need to be modified to exclude the volume occupied by clouds, and the resulting expressions would be different for the nondissipated (cylindrical cocoon) and dissipated (spherical cocoon) regimes.

3.3.1. Nondissipated Jet

In the nondissipated case, where $v_h > v_c$, the vertical expansion of the cocoon is still determined by the head velocity as in the uniform case. Hence, the volume occupied by the cocoon gas is

$$V_c \approx (1 - f_V)\pi v_c^2 v_h t^3, \tag{18}$$

which is just the volume enclosed by the outer cocoon minus the volume occupied by clouds inside the cocoon. This assumes that the clouds are destroyed by the cocoon on a timescale longer than the relevant dynamical timescale (since flow inside the cocoon is subsonic), so that the clouds remain intact/static for much longer. Moreover, the expression for jet density in terms of cocoon pressure remains the same as in Equation (10). With these modifications, the expressions for the time evolution of the head and cocoon parameters become

$$v_h \approx 2(4\pi)^{-1/5}(1 - f_V)^{-1/5}\lambda^{-2/5}\left(\frac{L_j}{\theta_0^4 \rho_H t^2}\right)^{1/5} \tag{19a}$$

$$v_c \approx \sqrt{\frac{4}{3}}(4\pi)^{-1/5}(1 - f_V)^{-1/5}\lambda^{1/10}\left(\frac{\theta_0 L_j}{\rho_H t^2}\right)^{1/5} \tag{19b}$$

$$P_c \approx (4\pi)^{-2/5}(1 - f_V)^{-2/5}\lambda^{1/5}\left(\frac{\theta_0^2 L_j^2 \rho_H^3}{t^4}\right)^{1/5} \tag{19c}$$

$$R_j \approx \frac{(4\pi)^{1/5}}{\sqrt{2\pi}}(1 - f_V)^{1/5}\lambda^{-1/10} v_j^{-1/2}\left(\frac{\theta_0^8 L_j^3 t^4}{{\rho_H}^3}\right)^{1/10}. \tag{19d}$$

Notice that for $f_V \ll 1$ the cocoon velocity is very weakly dependent on $\lambda = \rho_{\rm eff}/\rho_H$ but the head velocity decreases with λ as $\lambda^{-2/5}$. Therefore, we expect the head to become progressively slower with denser clouds.

3.3.2. Jet Dissipation

It is straightforward to generalize the above scalings for the case when the jet is dissipated by clouds well within the cocoon (see Section 4.2.2). In this case, the cocoon can be assumed to be a hemisphere with radius r_c. It is easy to check that in both the nondissipated and dissipated regimes the cocoon aspect ratio (approximated by v_c/v_h) is the same,

$$\frac{v_c}{v_h} \approx \theta_0 \sqrt{\frac{\lambda}{3}} \approx \frac{\theta_{0,10}}{10}\sqrt{\lambda}, \tag{20}$$

so that even jets with a small opening angle can become dissipated in a medium with a sufficiently large density contrast, λ (Equation (15)), between the clouds and the diffuse medium. For a half-opening angle of 10°, this model predicts that the jet becomes dissipated for $\lambda \equiv \rho_{\rm eff}/\rho_H \gtrsim 100$. Using numerical simulations, in Section 4.1 we show that a jet in a uniform medium indeed drives a self-similar cocoon+shock, but the ratio of cocoon to head speed is $2\times$ larger than the value given by Equation (20) (see Equation (25)), implying a $4\times$ smaller density threshold λ for dissipation. The scale of the cocoon properties is given by the analytic scalings, but the prefactors must be determined from numerical simulations (see Section 4).

3.3.3. Uniformly Distributed Clouds

The simplest realization of a clumpy medium is a uniform medium with randomly distributed clouds of a given radius, $R_{\rm cl}$, and volume filling fraction, f_V. Computing the effective density that the jet beam interacts with ($\rho_{\rm eff}$) for a general distribution of these clouds (having density $\rho_{\rm cl}$) is challenging because of the complex jet–cloud interaction. However, a physically motivated ansatz based on important dimensionless parameters of the problem for $\lambda \equiv \rho_{\rm eff}/\rho_H$ (assuming cold jet and medium) is

$$\frac{\rho_{\rm eff}}{\rho_H} = \lambda\left(\frac{\rho_{\rm cl}}{\rho_H}, f_V, \frac{R_{\rm cl}}{R_j}\right), \tag{21}$$

where the precise form of this function is unknown but will be calibrated with simulations in Section 4.2. The dependence on jet properties in Equation (21) goes into the jet radius R_j. Note that we can construct more dimensionless parameters, but $\rho_{\rm cl}/\rho_H$, f_V, and $R_{\rm cl}/R_j$[10] appear to be most relevant. In our simulations with variation of $R_{\rm cl}$, we find that λ is insensitive to $R_{\rm cl}$. However, this ansatz needs to be tested more closely with further numerical simulations.

We can further simplify things by separating the dependence on cloud density ($\rho_{\rm cl}$) and the cloud pattern (f_V, $R_{\rm cl}/R_j$). For this, we model the head to be obstructed by a medium of density $\rho_{\rm cl}$ (clouds) for a fraction f_L of the path length and ρ_H for a fraction $(1-f_L)$ of the path length. Consider a column of length L, which is large compared to the separation between clouds but small compared to the jet's total length, z_h. The time taken to traverse this distance (using Equation (3)) is given by

$$\begin{aligned} t &= \left(\frac{L}{v_j\sqrt{\rho_j}}\right)\left(f_L\sqrt{\rho_{\rm cl}} + (1-f_L)\sqrt{\rho_H}\right) \\ &\equiv \left(\frac{L}{v_j\sqrt{\rho_j}}\right)\sqrt{\rho_{\rm eff}}. \end{aligned} \tag{22}$$

This expression gives the required expression for $\lambda = \rho_{\rm eff}/\rho_H$ as

$$\lambda = \left(f_L\sqrt{\frac{\rho_{\rm cl}}{\rho_H}} + (1-f_L)\right)^2, \tag{23}$$

so that the unknown cloud length fraction, f_L, is only a function of the spatial distribution and size of the clouds. That is, for our setup

$$f_L \equiv f_L\left(f_V, \frac{R_{\rm cl}}{R_j}\right). \tag{24}$$

Here we assume that the only relevant dimensionless parameters determining f_L are cloud volume fraction (f_V) and the ratio of the cloud and jet radii ($R_{\rm cl}/R_j$). Thus, we have separated the dependence of λ on density contrast ($\rho_{\rm cl}/\rho_H$) and cloud size ($R_{\rm cl}$) and distribution (f_V).

Although a simple length-to-volume relation should be $f_L \propto f_V^{1/3}$ (independent of $R_{\rm cl}$), the calculation of f_L for any given cloud pattern from first principles is still difficult for several reasons. For example, there are large uncertainties associated with modeling the interaction between a jet and a single cloud, such as the distance over which a single cloud gets dragged before being destroyed, and the contribution due to the overlap of wakes of different clouds is not known accurately in general. In some cases, the expanding forward shock could preshock and destroy a cloud partially before the jet head interacts with it. Such processes depend on the cloud radius, $R_{\rm cl}$, which could be a parameter deciding f_L (and hence the assumed $R_{\rm cl}$ dependence). To make further progress, we use numerical simulations with varying cloud patterns (holding the cloud density fixed) to calibrate the functional dependence of f_L on f_V and $R_{\rm cl}/R_j$ in Section 4.2.1.

4. Results

In this section, we present the results from our numerical simulations of jets in a uniform and clumpy medium and compare them with analytic estimates obtained in Section 3. First, we compare the analytical predictions using a simulation of a jet propagating in a uniform medium (Section 4.1). While the scaling with time of cocoon radius and jet head location follow the analytic estimates, the exact prefactors differ. Following this, we verify our model using analytic scalings with jet simulations in a clumpy medium. However, due to the uncertainties in estimating the geometrical length factor f_L from first principles, in Section 4.2.1 we first perform simulations keeping cloud density constant and varying the pattern of clouds (i.e., their f_V and $R_{\rm cl}$) to study the dependence of f_L on f_V and $R_{\rm cl}$. Using the f_L value inferred from these simulations, we finally test the predictions of our calibrated model for the scaling of the head velocity v_h with the effective density encountered by the jet ($\rho_{\rm eff}$) in Section 4.2.2 by choosing a

[10] Cloud radius $R_{\rm cl}$ can be normalized with other length scales such as r_c and z_h, but the jet velocity (see Equation (22)) and its radius should affect jet–cloud interaction more directly.

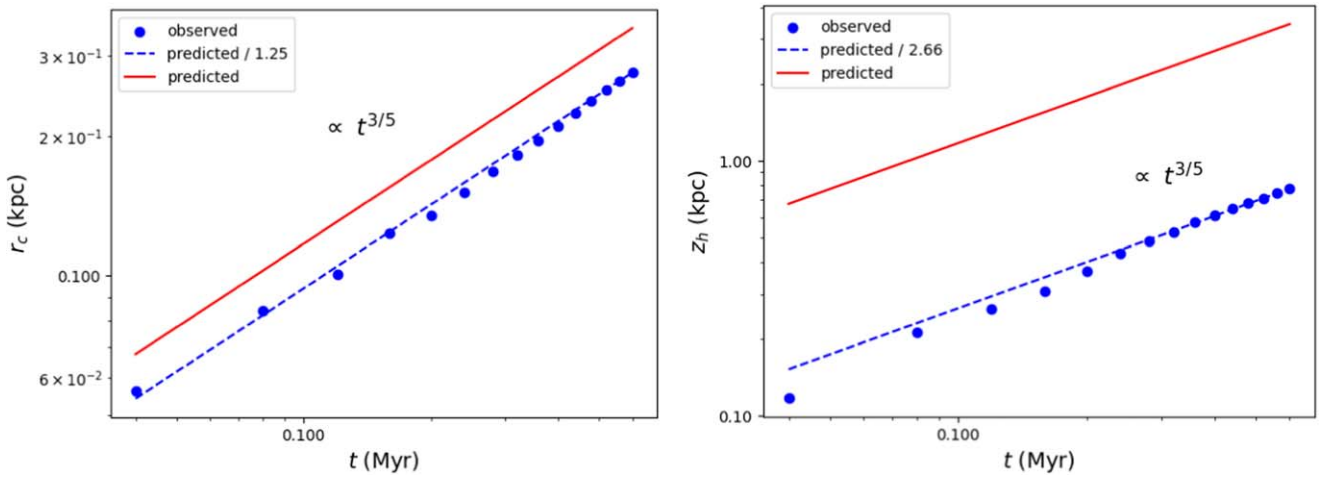

Figure 3. Blue circles show the measured values of cocoon radius r_c (left panel) and z_h (right panel) at different times for our uniform run (see Table 2). Red lines show the predicted values from the analytical model (integrating Equations (11b) and (11a)). Blue dashed lines show the predicted values scaled to match the observed values at $t \approx 0.6$ Myr.

fixed cloud pattern (fixed f_L) and varying the cloud density ($\rho_{\rm cl}$).

4.1. Analytical Model versus Simulations for a Uniform Medium

Here we compare the analytic model of propagation of a nonrelativistic jet in a uniform medium (Equations (11a) and 11b)) with results from numerical simulation, using the jet/ISM parameters listed in Table 1 and a cubic box of side $L_{\rm box} = 0.8$ kpc. We can follow the jet's evolution up to a time of 0.6 Myr, after which the jet head exits the domain (see Figure 2).

The time evolution of the cocoon lateral size (r_c) and the jet head position (z_h) are shown in Figure 3. The predicted values for these are obtained by integrating Equations (11b) and (11a) from 0 to t. For both the head and the cocoon, the predicted scaling with time of r_c, $z_h \propto t^{3/5}$ agrees with the simulation results. However, the predicted numerical prefactors are larger by a factor of 1.25 for r_c and by a factor of 2.66 for z_h. There are several possible reasons for this discrepancy. The jets are not purely kinetic energy driven in the simulations. Figure 2 shows that after the collimation shock the jet is no longer a laminar-type flow and rather contains turbulent structures. Such structures reduce the jet's directional ram pressure, resulting in a smaller height for the jet head. Moreover, the jet contains significant thermal energy after collimation (see the middle panel of Figure 2), in contrast to the assumption of a cold jet in the analytical model. The expressions (Equations (11a)–(13)) should have prefactors that depend on the gas adiabatic index (γ), but we have substituted $\gamma = 5/3$ relevant for our nonrelativistic jets. Additionally, the geometries of the jet and the cocoon outer shock, which we have assumed to be cylindrical in the analytical model, are not so in simulations (cocoon shapes for active and off jets are studied in Hardcastle & Krause 2013; Guo 2015; Yates-Jones et al. 2021). In addition, the model assumes a self-similar solution at all times, but this is likely to be broken at early times, e.g., when the jet collimation has not yet been completed. The model does not account for this early phase of jet launching. Previous studies of relativistic jets (Harrison et al. 2018) have highlighted the need for calibrating the analytical models of jet propagation derived from Bromberg et al. (2011) via numerical simulations.

The ratio of cocoon size to the jet vertical extent (using the calibration from our jet simulation in a uniform medium) is found to be

$$\frac{r_c}{z_h} = \frac{v_c}{v_h} \approx 1.23\ \theta_0 \approx 2.15 \times \frac{\theta_{0,10}}{10}, \tag{25}$$

assuming that the scaling of this ratio with θ_0 remains unchanged (see Equation (20) with $\lambda = 1$). Further assuming that the scaling of this ratio with the density contrast, λ (Equation (15)), is unchanged, this ratio in a clumpy medium should be

$$\frac{r_c}{z_h} = 2.15 \times \frac{\theta_{0,10}}{10}\ \sqrt{\lambda}. \tag{26}$$

Therefore, we obtain a prediction for the critical value of λ required for jet dissipation (i.e., $r_c = z_h$),

$$\lambda_{\rm crit} = \frac{21.7}{\theta_{0,10}^2}, \tag{27}$$

above which the jet will be dissipated.

Figure 2 shows the snapshots of the density (left panel), pressure (middle panel), and vertical velocity (right panel) for our uniform-medium run. Clearly, the cocoon geometry is far from cylindrical (cocoon shape depends on background density profile; see, e.g., Figure 3 in Harrison et al. 2018), and z_h/r_c is smaller than $\sqrt{3}/\theta_0 \approx 10$, the value expected from self-similar theory (see Equation (20) with $\lambda = 1$). This small discrepancy is also observed in earlier relativistic simulations (Harrison et al. 2018), but Figure 3 shows that the evolution follows the same time dependence as estimated in the analytical theory (Section 3.1).

In Figure 2, one can clearly see the jet collimation shock, an almost cylindrical jet beam with a turbulent surface, a high-velocity backflow in the inner cocoon, and a dense outer cocoon with Kelvin–Helmholtz vortices at the inner edge. The pressure is roughly uniform in the cocoon because of the high temperature and the associated large sound speed compared to the flow speeds. Most galaxy formation simulations (especially large-volume cosmological simulations of populations of galaxies), with resolutions insufficient to resolve the jet radius (see Equation (13)), of low-power jets $\lesssim 10^{42}$ erg s^{-1} cannot

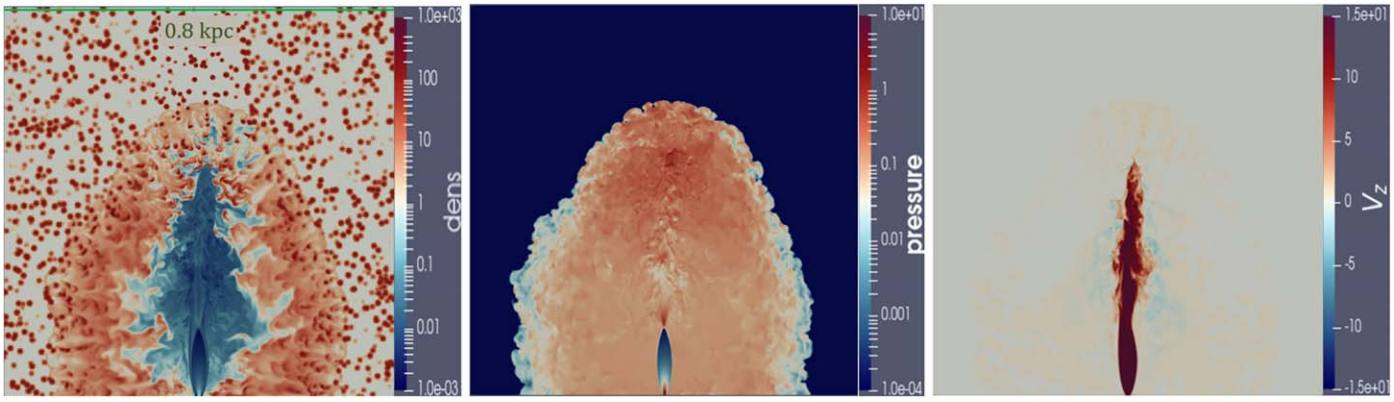

Figure 4. 2D slices (y-z plane) of density (m_p cm^{-3}; left), pressure (1.67×10^{-8} dyn cm^{-2}; middle), and vertical velocity (1000 km s^{-1}; right) for a jet in a medium with $\rho_H = 1 m_p$ cm^{-3}, $\rho_{\rm cl} = 100 m_p$ cm^{-3}, and $f_V = 0.1$, at time $t = 0.96$ Myr. Note that even though many of the clouds inside the cocoon are largely intact (since destruction time inside the cocoon is long), they have already come in pressure equilibrium with the cocoon, as the shock driven by the high-pressure cocoon can compress these clouds on timescales ∼0.1 Myr (see text around Equation (28)). The backflows with clouds are weaker than in the uniform case shown in Figure 2.

capture, even qualitatively, the evolution of the cocoon and energy dissipation by AGN jet feedback (see Section 5.4 for further discussion).

4.2. Jets in a Clumpy Medium

Clumps affect the cocoon scalings because of the different responses of the jet and cocoon to clouds, as discussed in Section 3.3. The expressions for the head and cocoon velocities in a clumpy medium (Equations (19a) and (19b)) and in a uniform medium (Equations (11a) and (11b)) have a very similar form but have additional dependence on $\lambda = \rho_{\rm eff}/\rho_H$ and a weak dependence on f_V. Here λ itself depends on $\rho_{\rm cl}/\rho_H$, f_V, and $R_{\rm cl}/R_j$ (Equation (21)), which can be further decomposed into the dependence on the cloud density contrast ($\rho_{\rm cl}/\rho_H$) and the cloud pattern (f_V, $R_{\rm cl}/R_j$; see Equations (23) and (24)). Now, through numerical simulations, we decouple the dependence on the cloud pattern (Section 4.2.1) and on the cloud density (Section 4.2.2).

Important timescales for clouds within the cocoon. Before describing results from simulations of jets interacting with a clumpy ISM, we estimate some timescales that help us understand the dynamics of clouds within the cocoon not directly interacting with the jet beam. Note that the sound crossing time across the clouds

$$t_{s,\rm cl} \equiv \frac{2R_{\rm cl}}{c_{s,\rm cl}} = 6.7 \ \ {\rm Myr}\, R_{\rm cl,\,5} T_{H,4}^{-1/2} \sqrt{\frac{\rho_{\rm cl}/\rho_H}{100}}, \qquad (28)$$

where $R_{\rm cl,5}$ is the cloud radius normalized to 5 pc and $T_{H,4}$ is the temperature of the homogeneous ISM in units of 10^4 K. Since this timescale is much longer than the dynamical time, the clouds are expected to be isochoric and underpressured just after the passage of the forward shock. The underpressured clouds are expected to implode on a timescale $t_{\rm imp} \sim R_{\rm cl}/\sqrt{P_c/\rho_{\rm cl}} \sim t_{s,\rm cl}(P_H/P_c)^{1/2} \sim 0.02$ Myr, much shorter than the sound crossing time (P_H is the ISM pressure). Simultaneously, clouds are being mixed by shear instabilities on a $t_{\rm cc} \sim R_{\rm cl}(\rho_{\rm cl}/\rho_c)^{1/2}/v_c$ timescale, which can be longer than the implosion time by $\sim\sqrt{\rho_H/\rho_c}$ within the inner cocoon (assuming the relative velocity everywhere within the cocoon $\sim v_c$). Thus, the clouds embedded in the hot cocoon are compressed, mixed, and pushed (due to the motion of the cocoon material relative to the clouds). Also note that the cocoon velocity and its pressure are changing on a dynamical time (Equations (11c) and (11b)). Because of these various complexities, quantitatively predicting cloud evolution within the cocoon is difficult.

Figure 4 shows the snapshots of density, pressure, and vertical velocity for our fiducial clumpy run f01R5. The dense shell is much thicker because of the mixing of clouds into the shell. The clouds near the outer periphery of the dense shell are underpressured but become isobaric inside the cocoon, consistent with the estimate in the previous paragraph. The backflow in the inner cocoon is irregular and less prominent. Most importantly, the cocoon is more spherical than the one in a uniform medium shown in Figure 2.

4.2.1. Effect of Different Cloud Pattern (f_V, R_{cl})

In this subsection, we present runs from which we can deduce the dependence of the effective length fraction of clouds encountered by the jet (f_L) on the cloud volume fraction (f_V) and the cloud size ($R_{\rm cl}$; see Table 2 for the list of these runs), before exploring the $\rho_{\rm cl}/\rho_H$ dependence in Section 4.2.2. Therefore, here we study the effect of varying the number and size of clouds (keeping $\rho_{\rm cl}$ constant at $100 m_p$ cm^{-3}) on the head and cocoon dynamics. For this, we perform simulations with a wide range of volume filling fractions ranging from 0.00625 to 0.1 and cloud radii between 5 and 10 pc. We fix individual cloud positions to avoid statistical fluctuations because of the random positioning of clouds across these runs. Some clouds are then removed to reduce f_V and/or to increase $R_{\rm cl}$ (see Figure 1). Snapshots of density for simulations with constant $R_{\rm cl}$ but varying f_V are shown in Figure 5, while those with constant f_V but varying $R_{\rm cl}$ are shown in Figure 6. The figures indicate that the volume filling fraction significantly affects the cocoon size and shape, whereas the cloud radius only has a mild effect. Therefore, one can qualitatively expect that f_L (and therefore λ) does not significantly depend on the cloud size (as long as f_V remains the same). In all cases, the cocoon engulfs the clouds, partially disrupted by the dense shell but not much affected once inside the lower-density inner cocoon. The smaller clouds (due to a shorter cloud-crushing time) and clouds with larger volume

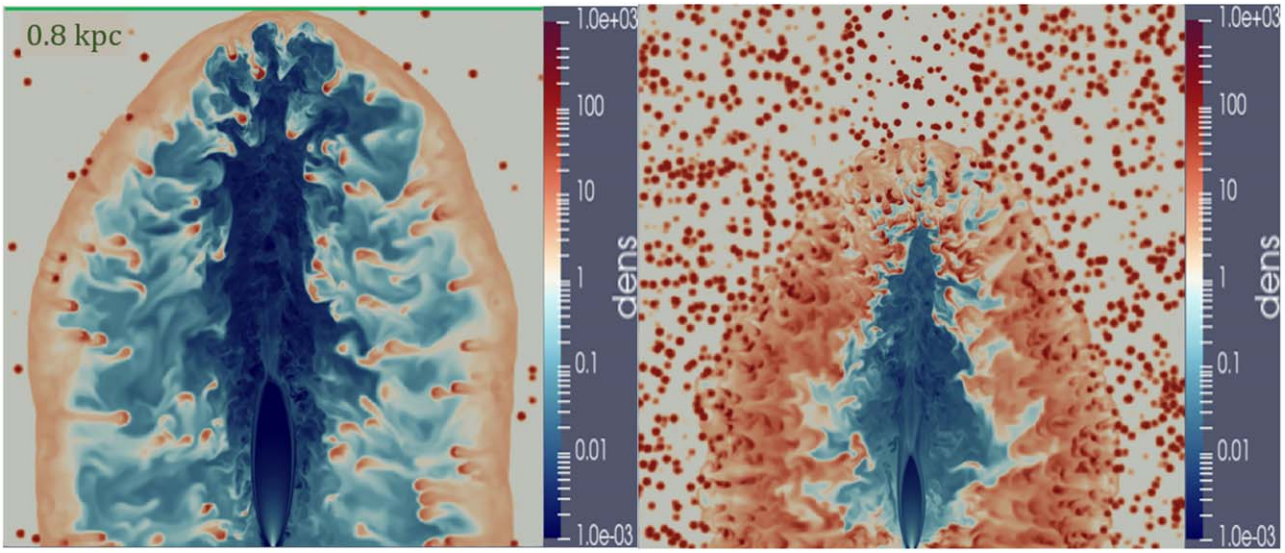

Figure 5. Snapshots of density in the y-z plane for cloud density of $100 m_p\,\mathrm{cm}^{-3}$, $R_{\rm cl} = 5$ pc, and $f_V = 0.00625$ (left panel) and $f_V = 0.1$ (right panel), at time $t = 0.96$ Myr. As expected, the cocoon is more spherical and dissipated for a higher volume fraction of clouds.

filling fraction (since material from many clouds is shredded) mass-load the shocked ISM shell.

This set of simulations is designed to capture the transition from the highly nondissipated regime (very few or no clouds) to the near-dissipated regime (large f_V). The cocoon expansion velocity in Figure 7 shows very little variation across all runs, as expected (from Equation (19b)), and stays at around $300\,\mathrm{km\,s^{-1}}$. Figure 7 shows that the head velocity decreases rapidly with increasing f_V for small f_V and then saturates (or decreases very slowly) at around $400\,\mathrm{km\,s^{-1}}$ for $f_V \gtrsim 0.02$. Note that none of the runs in Table 2, except for $R_{\rm cl} = 10$ pc and $f_V = 0.1$ for which $v_h < v_c$ (see Figure 7), are fully dissipated since $v_h > v_c$. However, for $f_V \gtrsim 0.02$ there is no prominent jet head and at least a few clouds are obstructing the jet beam within the vertical extent of the cocoon (right panels of Figures 5 and 6). There is a continuous decrease in the average head velocity with increasing f_V before it decreases below the cocoon's lateral expansion velocity and the jet dissipates. The figure also shows the simulations with the same f_V but different cloud radii. We find that the cloud radius does not have much effect on the cocoon dynamics, and f_V is the important parameter governing f_L and $\rho_{\rm eff}$.

Now, based on the head velocities measured here and the equations of the analytical model (Equations (19a) and (23)), we can compute a value of f_L for each of these simulations. For this, we note that in the case of a uniform medium $\lambda = 1$. Then, using Equation (19a) (neglecting the $(1 - f_V)$ dependence as $f_V \ll 1$), we obtain

$$\lambda = \frac{\rho_{\rm eff}}{\rho_H} = \left(\frac{v_h}{v_{h,\rm uniform}}\right)^{-5/2}, \tag{29}$$

which gives us the required $\rho_{\rm eff}$ for several combinations of f_V and $R_{\rm cl}$. Substituting this $\rho_{\rm eff}$ in Equation (23), we can solve for f_L as

$$f_L = \frac{\sqrt{\rho_{\rm eff}} - \sqrt{\rho_H}}{\sqrt{\rho_{\rm cl}} - \sqrt{\rho_H}}. \tag{30}$$

A plot of the f_L values thus obtained as a function of f_V is shown in Figure 8. We observe that f_V is the major factor in controlling f_L; changing $R_{\rm cl}$ at the same f_V does not change f_L significantly.[11] Except for the $(f_V,\ R_{\rm cl}) = (0.1,\ 10\,\mathrm{pc})$ run, which appears to be an outlier, there is no systematic variation of the head and cocoon speeds with the cloud size. This outlier value may be due to the small number of clouds along the jet's path. In Figure 8, f_L increases sharply from 0 with increasing f_V and then grows slowly to values of $\approx$0.2–0.3 for $f_V \gtrsim 0.02$. For example, for $(f_V,\ R_{\rm cl}) = (0.1,\ 5\ \mathrm{pc})$, f_L is found to be 0.28. We find that a scaling

$$f_L = 0.6\, {f_V}^{1/3} \tag{31}$$

fits the data quite well (solid line in Figure 8), as expected. The normalization factor is, however, nontrivial to obtain from first principles since it involves complex jet–cloud interactions as noted in Section 3. Of course, this scaling (and other assumptions of our model) will break down as f_V approaches unity (and f_L approaches 0.6). Now, for $\rho_{\rm cl}/\rho_H = 100$ and $f_V = 0.1$, $f_L = 0.6 f_V^{1/3} = 0.28$, and Equation (23) gives $\lambda = 12.4$, which is $< \lambda_{\rm crit}$. Thus, none of the simulations in Table 2 (except f01R10, which has a large outlier $f_L = 0.41$) are expected to be fully dissipated, consistent with Figure 7. Note that for f01R10 there are about 8 times fewer clouds than our other simulations. The interaction of the jet with a small number of clouds could suffer from statistical fluctuations and, therefore, be an outlier to the fitted curve.

4.2.2. Effect of Different Cloud Density (ρ_{cl})

With the values of the effective length fraction covered in clouds (f_L) inferred from Section 4.2.1, we are now in a position to determine $\rho_{\rm eff}$ for a given pattern $(f_V,\ R_{\rm cl})$ and density of clouds ($\rho_{\rm cl}$). Thus, we can now test the predicted scaling of v_h

[11] While we have varied f_V by more than two orders of magnitude, we could vary the cloud size only within a factor of 2. Smaller clouds become numerically unresolved, and with larger clouds the number of clouds along the jet beam is small, and there is a large statistical variation in simulation outcomes. The length fraction f_L may depend on $R_{\rm cl}$ for a larger range of variation, but we do not explore this here.

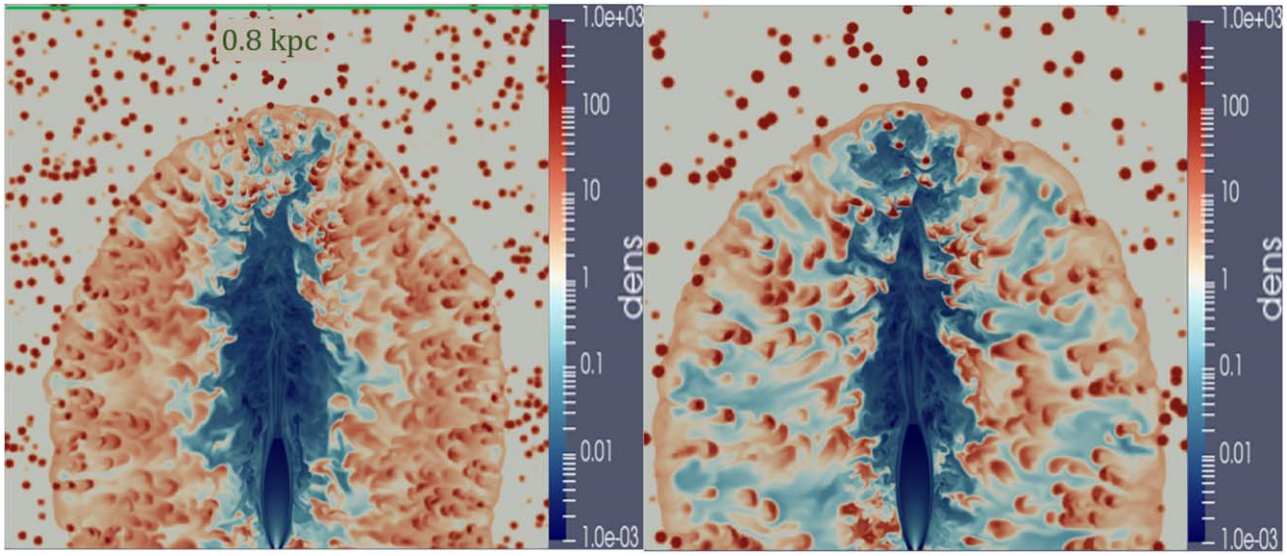

Figure 6. Snapshots of density in the y-z plane for cloud density of $100m_p\,\mathrm{cm}^{-3}$, $f_V = 0.05$, and $R_{\rm cl} = 5$ pc (left panel) and $R_{\rm cl} = 7.9$ pc (right panel), at time $t = 0.96$ Myr. The two cocoons have a similar aspect ratio (see Figure 7) and are not dissipated. Smaller clouds (left panel) are disrupted more compared to larger ones (right panel) and mass-load the shocked ISM.

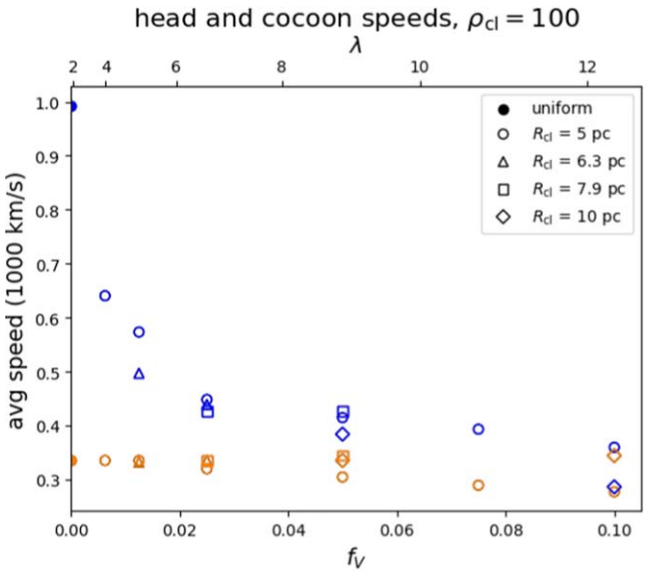

Figure 7. Variation of the average head velocity (v_h; blue) and average cocoon velocity (v_c; orange) as a function of f_V for $\rho_{\rm cl} = 100m_p\,\mathrm{cm}^{-3}$. Different symbols correspond to different cloud sizes $R_{\rm cl}$. For $f_V \gtrsim 0.02$, the average head speed decreases very slowly with f_V. The λ values shown on top are derived from Equation (32).

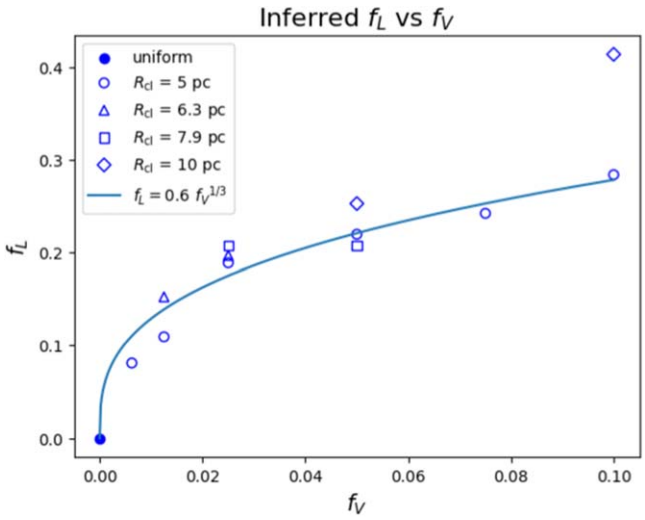

Figure 8. Variation of the effective cloud path length f_L (as inferred from our numerically calibrated analytical model, Equation (30)) as a function of f_V, for the same set of simulations shown in Figure 7. The solid line shows a fit $f_L = 0.6 f_V^{1/3}$ that matches the simulation results; the $R_{\rm cl} = 10$ pc and $f_V = 0.1$ run may be an outlier, due to very few clouds along the jet beam.

and the ratio $\lambda\,(\rho_{\rm eff}/\rho_H)$ by fixing a particular cloud pattern (with f_L inferred from Equation (31)) and varying the density of the cloud material. In this section, we present the results for jet head and cocoon dynamics from the simulations where the distribution of clouds is held fixed at $(f_V, R_{\rm cl}) = (0.1, 5\ \mathrm{pc})$ and cloud density is varied from $12m_p$ to $100m_p\,\mathrm{cm}^{-3}$ (see Table 3). For this cloud distribution, we find f_L to be 0.284 in Section 4.2.1 for $\rho_{\rm cl} = 100m_p\,\mathrm{cm}^{-3}$, and we assume the same value of f_L for all cloud densities. We use this value of f_L to compute $\rho_{\rm eff}$ corresponding to each value of $\rho_{\rm cl}$, using Equation (23). Snapshots of density for the two extreme cases ($\rho_{\rm cl} = 12$, $100m_p\,\mathrm{cm}^{-3}$ or, $\lambda = 2.9$, 12.65) are shown in Figure 9.

Cocoon expansion. We begin with a study of the lateral extent of the cocoon, r_c. As expected, the cocoon expands through the warm phase quite smoothly with time. Thus, we can study both the time dependence of r_c and the dependence of the average cocoon expansion velocity (v_c) on the cloud parameters.

For the time dependence of r_c, our analytic model (Section 3) predicts that the instantaneous velocity in all regimes scales as $v \propto t^{-2/5}$. Integrating this, we obtain the prediction that $r_c \propto t^{3/5}$. From the plots of r_c against time, shown in Figure 10, we observe that the scaling is indeed close to the predicted value of 0.6. Moreover, the dependence of the cocoon velocity on cloud density (for a fixed density of the diffuse medium ρ_H) is very weak, consistent with Equation (19b). The model predicts that in the nondissipated regime $v_c \propto \rho_{\rm eff}^{1/10}$ and in the dissipated regime $v_c \propto \rho_{\rm eff}^{0}$ (since our simulations were performed keeping ρ_H fixed, $\rho_{\rm eff}$ is proportional to λ). Such weak dependence is

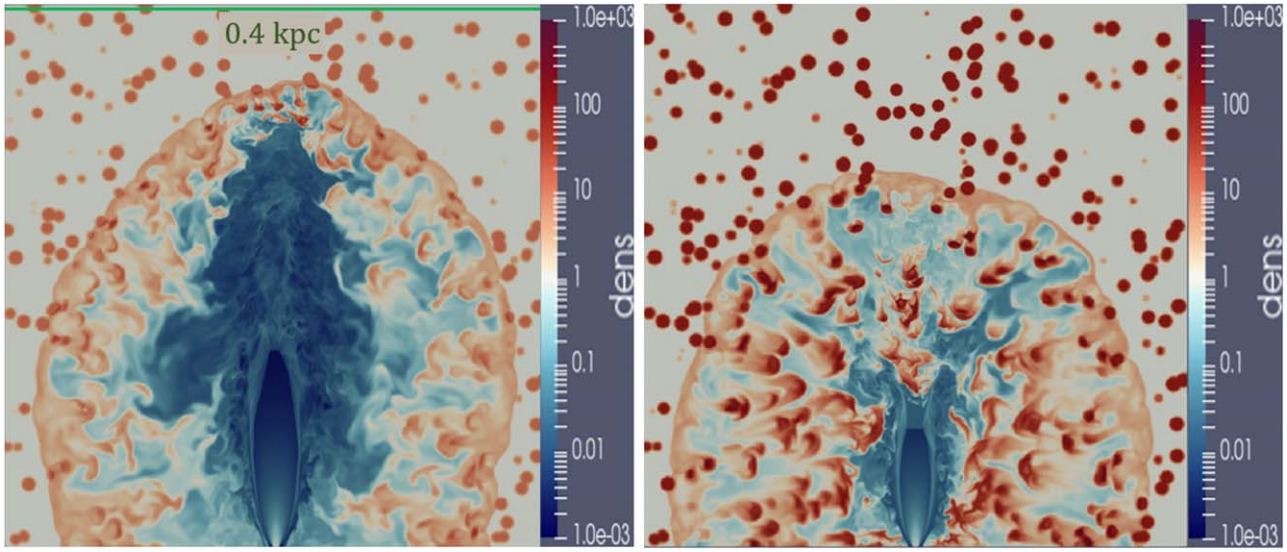

Figure 9. Snapshots of density for $f_V = 0.1$ and cloud densities of $12m_p$ cm^{-3} ($\lambda = 2.9$) (left panel) and $100m_p$ cm^{-3} ($\lambda = 12.6$) (right panel), at time $t = 0.56$ Myr, which represent the nondissipated and fully dissipated regimes, respectively. For the former jet power dissipates at the clouds close to the vertical cocoon boundary, whereas for the latter the jet beam is obstructed by clouds well within the cocoon.

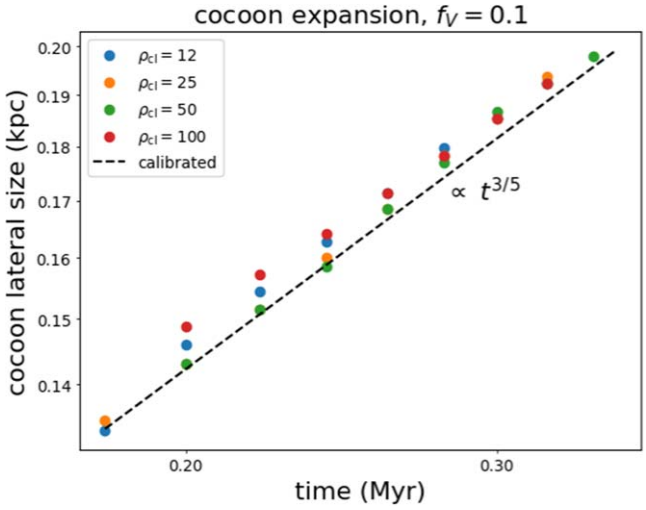

Figure 10. The time evolution of the cocoon size (r_c) for $f_V = 0.1$. The cloud densities correspond to $12m_p$, $25m_p$, $50m_p$, and $100m_p$ cm^{-3}. These agree with the predicted scaling of $r_c \propto t^{3/5}$, and there is a very weak dependence on the cloud density. The dashed line shows the calibrated scaling for the cocoon radius from the left panel of Figure 3.

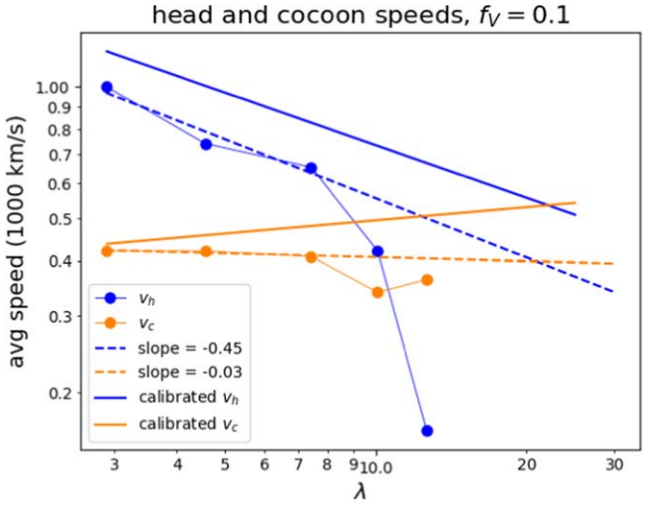

Figure 11. The markers show average head and cocoon velocities (v_h and v_c) as a function of λ for runs in Table 3 with $f_V = 0.1$. The cloud densities are $\rho_{cl} = 12m_p$, $25m_p$, $50m_p$, $75m_p$, and $100m_p$ cm^{-3}. The solid lines show the speeds expected from our calibrated model for the jet head (blue; Equation (19a)) and cocoon (yellow; Equation (19b)), and the dashed lines are the power-law extrapolations of the simulation data. The head velocities are in good agreement with the predicted scaling of $v_h \propto \rho_{\rm eff}^{-2/5}$ in the nondissipated regime (Equation (19a)).

difficult to verify with simulations. However, we do confirm (from Figure 11) that the average v_c stays almost the same (about 400 km s^{-1} before the cocoon leaves the box) over a large range of $\rho_{\rm eff}$ values (somewhat larger than values in Figure 7 because of an earlier time here for a smaller box).

Jet head propagation. Since the dependence of cocoon expansion on the clumpiness of the medium (parameterized by λ) is quite weak, it is clear that the increase in jet dissipation with increasing λ is largely due to the slowing down of the jet head velocity, v_h. Since instantaneous v_h in a clumpy medium can vary rapidly as the head interacts intermittently with clouds, comparing its time evolution in simulations with analytic estimates is difficult. Hence, we focus on the time-averaged v_h obtained from the simulations, in particular its dependence on $\rho_{\rm eff}$. The time-averaged head velocity is estimated as $v_h = (z_h(t_2) - z_h(t_1))/(t_2 - t_1)$, where we consider t_1 to be the time right after the jet is fully collimated and t_2 to be the time right before the cocoon material leaves the simulation box.

In the nondissipated regime, the model predicts that the average head velocity should scale as $v_h \propto \rho_{\rm eff}^{-2/5}$. This is quite close to the results obtained from the simulations for low-density clouds, as shown in Figure 11. By extrapolating the scalings obtained in the nondissipated regime, the critical value of λ required for jet dissipation is found to be $\approx$20 (see Figure 11), which is in good agreement with the calibrated prediction of 21.7 (Equation (27)). However, we note that $v_h < v_c$ happens about a factor of 2 earlier than expected. We suspect that the reason for this shift is the lack of a hollowed-out region at the jet base for this set of simulations compared to

the simulations used to calibrate v_h and v_c (Sections 4.1 and 4.2.1). This presence of dense clouds at the jet base delays jet collimation, invalidating the key assumption of our analytic models. However, such effects become apparent only close to the dissipation regime. This indicates that our criterion for the jet dissipation, i.e., $\lambda_{\rm crit} \sim 20$, may require some revision for a realistic ISM.

While the simulations presented in this section show that the critical value of λ may reduce (by a factor of 2) owing to dense clouds in the immediate surroundings of the jet base, the distribution of dense ISM is uncertain for several reasons. First, the local clouds may be evacuated by local supernova activity or be arranged in a ringlike/disklike fashion owing to tidal interactions and angular momentum at the galactic centers (Anglés-Alcázar et al. 2021). For our oversimplified clumpy ISM, with a larger simulation domain, we expect the influence of the delayed formation of collimation shock to reduce and an even closer match with the (calibrated) analytic prediction for jet dissipation. These runs also show the limitations of numerical simulations (because of finite resolution and small box size) in capturing all the relevant physics quantitatively.

5. Astrophysical Implications

The primary motivation for this work was to extend the analytic scalings developed for self-collimated jets propagating through a smooth ambient medium (following Bromberg et al. 2011) to the simplest model of a clumpy medium. The clumpiness of the ISM plays an important role in jet–ISM/CGM interaction. Our analytic scalings can help apply the simulation results across a range of parameters in jet power, jet opening angle, ambient density, etc. In the following, we discuss our study's caveats and astrophysical implications and compare them with related works.

5.1. Jet Dissipation Criterion in a Clumpy Medium

For a given clumpy medium having cloud density $\rho_{\rm cl}$, volume filling fraction f_V, and cloud radius $R_{\rm cl} \approx 5$ pc, we describe here the procedure for computing the head and cocoon speeds according to our model. First, f_L is found using Equation (31) as $f_L = 0.6\, {f_V}^{1/3}$. Then, using Equation (23), we get

$$\lambda = \left(0.6\, {f_V}^{1/3} \sqrt{\frac{\rho_{\rm cl}}{\rho_H}} + (1 - 0.6\, {f_V}^{1/3})\right)^2. \tag{32}$$

This can then be used in equations such as Equations (19a) and (19b) to compute the time evolution of the jet head and cocoon.

Using this relation and the criterion for jet dissipation predicted by our calibrated model (Equation (27)), we can compute the predicted critical values of the cloud density contrast $\rho_{\rm cl}/\rho_H$ and f_L (or f_V), above which the jet will be dissipated. These threshold values are shown in Figure 12 for four choices of the initial opening angle of the jet, θ_0. This figure suggests an easy way to evaluate whether the jet is dissipated for given jet and ISM parameters.

5.2. Excluded Physics and Implications

To make progress analytically, we had to make extreme simplifications. We briefly mention the important physical effects we excluded and discuss their impact on jet–ISM +CGM interaction.

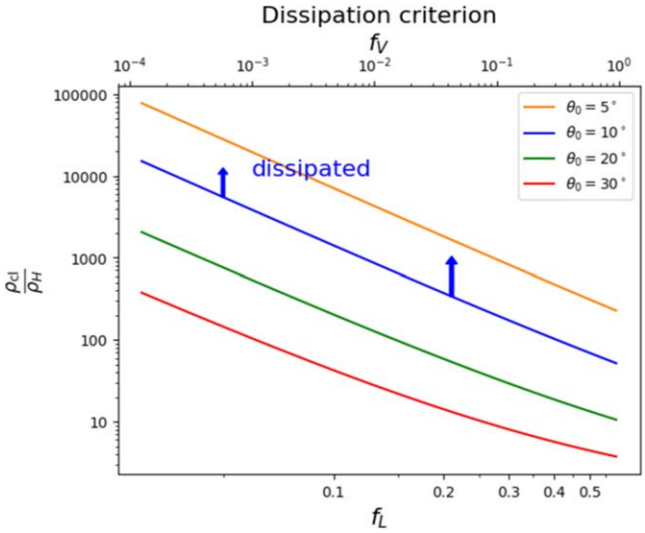

Figure 12. Curves showing the values of the cloud length fraction f_L and density contrast $\rho_{\rm cl}/\rho_H$ above which the jet would be dissipated for four choices of the initial opening angle θ_0, as predicted by our calibrated model, i.e., $\lambda_{\rm crit} = 21.7/\theta^2_{0,10}$ (Equation (27)). The f_V values (shown on top) corresponding to a given f_L are obtained through the relation $f_L = 0.6\, {f_V}^{1/3}$.

5.2.1. Radiative Cooling

Section 3.1 shows that the cocoon pressure collimates the conical jet into a cylindrical geometry. However, radiative cooling at various locations within the cocoon (shocked ISM, shocked jet, mixed clump–cocoon gas) can reduce the cocoon pressure. Among other effects, a reduced cocoon pressure can decollimate the jet into a conical shape (see Equation (8)).

The cooling time (for free–free and line cooling) in terms of the pressure and temperature is given by

$$t_{\rm cool} \sim \frac{3}{2}\frac{k_{\rm B}^2 T^2}{P\Lambda[T]} \sim 0.006\ {\rm Myr}\ T_6^2 P_{-9}^{-1} \Lambda_{-22}^{-1}, \tag{33}$$

where $T_6 = T[{\rm K}]/10^6$, $P_{-9} = P[{\rm dyn\ cm^{-2}}]/10^{-9}$, and $\Lambda_{-22} = \Lambda[{\rm erg\ cm^3\ s^{-1}}]/10^{-22}$ (see solid lines in Figure 7 of Kanjilal et al. 2021 for the variation of cooling time vs. temperature in isobaric and isochoric conditions). The cooling time scales inversely with the pressure. In the absence of cooling, the density of the shocked homogeneous ISM is $4\rho_H$, and the temperature of the outer cocoon is

$$T_{\rm oc} = \frac{\mu m_p}{4\rho_H}\frac{P_c}{k_{\rm B}} = 1.2 \times 10^6\ {\rm K}\frac{m_p {\rm cm^{-3}}}{\rho_H}\frac{P_c}{10^{-9}[{\rm dyn\ cm^{-2}}]}. \tag{34}$$

The outer cocoon cooling time is longer at earlier times, $\propto P_c \Lambda^{-1} \propto t^{-4/5}$ (assuming a weak dependence of Λ on T). The outer shock is expected to cool after $t > t_{\rm cool,oc}$, which is $\approx$0.05 Myr for our fiducial parameters. By this time, the head moves beyond $\sim v_h t = 330$ pc (assuming a uniform ISM) into the lower-density CGM, where cooling is weaker. However, the cocoon still moves into the dense ISM. After this, most jet energy can be carried into the CGM, which is not as clumpy and dense as the ISM. The jet's passage into the lower-density medium also leads to a sudden lateral expansion of the jet +cocoon (e.g., Sutherland & Bicknell 2007).

We note that while the dilute bubble contains most of the total energy of the jet+cocoon, the radiative shell can still lose the majority of the injected energy for a dense ISM (see, e.g., Figure 8 of Sharma et al. 2014 and Figure 14 of Yadav et al. 2017 for the importance of radiative losses in simulations of superbubble winds; see Oey 2009 for observational evidence).

Apart from the shocked ISM, the mixed gas around cold clouds within the cocoon can also cool. As noted in Section 4.2, our clouds are isochoric early on and implode to become isobaric on a $\gtrsim$0.02 Myr timescale (see middle panel of Figure 4). Here we assume the clouds to be roughly the same as their original density in the ISM (see the left panel of Figure 4). The cloud-crushing time for the clouds interacting with the jet head is much shorter than that of those embedded in the cocoon since the jet speed is much larger than the cocoon speed. The jet–cloud density contrast is $\sim\rho_{\rm cl}/\rho_j \sim \rho_{\rm cl}\theta_0^2 v_j^2/(4P_c) \sim (\theta_0^2/3)(\rho_{\rm cl}/\rho_H)(v_j/v_c)^2$ (see Equations (10) and (7)), which is $\sim$5000 at 1 Myr for our fiducial parameters. Hence, the cloud-crushing time for clouds in the head is $\sim\sqrt{5000}\,R_{\rm cl}/v_j \sim 0.02$ Myr. This time is longer for clouds interacting with the inner cocoon (rather than the jet) since the relative speed is smaller. The mixed gas (with a higher temperature) can be considered to have a temperature $\sim\sqrt{T_{\rm ic}T_{\rm cl}}$ (Begelman & Fabian 1990), where the inner cocoon temperature $T_{\rm ic} \sim \mu m_p P_c/(k_{\rm B}\rho_{\rm ic}) \sim \mu m_p v_j^2\theta_0^2/(4k_{\rm B}) \sim 10^8$ K (the inner cocoon density $\rho_{\rm ic}$ is assumed to be $\sim\rho_j$). Thus, the mixed gas is at $\sim10^5$ K, and the cooling time of this gas at the cocoon pressure is $\sim$6 yr (plugging $T_6 = 0.1$ and $\Lambda_{-22} = 10$ into Equation (33))! Since the cooling time of mixed gas is very short, loss of cocoon pressure happens on the mixing time $\sim t_{\rm cc} \sim (R_{\rm cl}/v_c)(\rho_{\rm cl}/\rho_c)^{1/2} \gtrsim 0.05$ Myr (mixed gas in the inner cocoon has even longer cooling time) rather than the cooling time of the mixed gas. Thus, both the cooling of the shocked ISM and that of the mixed gas, as well as subsequent loss of cocoon pressure, start to happen after 0.05 Myr. Although the volume occupied by mixed gas is small, it may still radiate away most of the cocoon thermal energy because of high radiative efficiency. For relativistic jets the cocoon temperature would be much higher (and the mixed gas density would therefore be much lower), so the cooling times can be much longer.

Note that our estimates are very crude and must be tested with radiative jet–ICM simulations. Despite radiative cooling losses, our analytic framework can still be used by replacing the jet luminosity L_j in analytic estimates by ηL_j, where $\eta < 1$ is an efficiency factor that accounts for radiative losses.

Also worth noting is the effect of an overpressured cocoon on the cloud. With radiative cooling, the cloud would become highly compressed as it tries to stay at a constant temperature because of efficient cooling in an overpressured cocoon. This leads to a collapse of the cloud to high densities (and possible fragmentation; see Zubovas et al. 2014), potentially causing localized enhanced star formation, which could contribute to positive feedback from AGN jets.

If the jet can drill through the dense ISM before it switches off, it is not expected to choke owing to catastrophic radiative losses in the dense ISM. The Compton cooling time for the cocoon with cosmic microwave background and stellar light as seed photons is much longer (we assume the central AGN to have a luminosity much smaller than the Eddington limit, as appropriate for most nearby AGN). The electron–proton energy equipartition time and the radiative recombination time for the dense/mixed gas are short, so that the equilibrium cooling function can be used. Extending our simulations to include cooling and realistic ISM+CGM gas distribution will be most interesting.

5.2.2. Disk–CGM Transition: Comparison with J1316+1753

The other unrealistic simplifications we have made for ease of analytic treatment are statistical homogeneity and isotropy. In reality, the warm/cold (10^4/100 K) ISM is strongly stratified, with the disk scale height much smaller than the radial scale length. In a stratified ISM, once the cocoon expands beyond a disk scale height, it accelerates vertically and slows its expansion into the disk. After this, the cocoon energy is preferentially deposited in the less dense/nonradiative CGM, and our assumption of a uniform medium breaks down even qualitatively. Our scalings tell us when we expect the cocoon to break out of the ISM disk.

Numerical simulations (Mukherjee et al. 2018; Tanner & Weaver 2022) show that even jets that are launched into the clumpy ISM disk at a large inclination angle create a bipolar outflow symmetric relative to the galactic center. Once the cocoon reaches close to the disk scale height, it takes the path of the lowest column along the galaxy minor axis. This is also consistent with multiwavelength observations (e.g., Venturi et al. 2021; Girdhar et al. 2022), which show the warm nebular gas with large velocity dispersion perpendicular to the ISM disk.

Applying our model to the J1316+1753 jet. Our formalism of the jet encountering a larger effective density compared to the cocoon (Section 3.3) can also be applied to a jet propagating into the ISM disk and the cocoon expanding into the lower-density warm/hot medium. Assuming that the jet is launched into the dense ISM disk, $\rho_{\rm eff} \approx \rho_{\rm mid} \sim 3\times10^4 m_p$ g cm^{-3} (the density in the ISM midplane) and $\rho_H \approx \rho_{\rm diffuse} \sim 100 m_p$ g cm^{-3}, where we quote the density estimates in nearby quasar J1316+1753 from Girdhar et al. (2022).[12] The molecular phase (at a few tens of kelvin) in the midplane is assumed to be in pressure equilibrium with the warm phase.

For J1316+1753, the jet head is well within the cocoon, which expands along the disk minor axis. For the anisotropic medium (within the disk plane vs. perpendicular to it) we consider here, the estimates in Section 3.3.1 are valid even for dissipated jets like J1316+1753 because the cocoon is preferentially moving into the low-density CGM and the jet head is obstructed by molecular gas in the disk. The length factor is expected to be $f_L \approx 1$ for a jet propagating into the molecular disk and thus $\lambda \equiv \rho_{\rm eff}/\rho_H \sim \rho_{\rm mid}/\rho_{\rm diffuse} \sim 300$. In addition, $f_V \ll 1$, since most of the cocoon volume is occupied by the diffuse warm phase away from the midplane. Assuming $L_j \approx 10^{44}$ erg s^{-1} (estimated from radio luminosity in Girdhar et al. 2022), the fiducial $\theta_0 \approx 10°$, $\rho_H \sim 100 m_p$ cm^{-3}, and the measured cocoon radius $r_c \sim 7$ kpc, we can calculate the age of this cocoon from integrating Equation (19b) and using the calibration from Figure 3 as $\sim$75 Myr (where we have plugged in $\lambda = \rho_{\rm mid}/\rho_{\rm diffuse} = 300$ in Equation (19b)). The numerically calibrated $r_c/z_h \approx 0.215\theta_{0.10}\lambda^{1/2}$ from Equation (25) with the measured $r_c/z_h \approx 7/1.5$ gives $\lambda \sim 470$. This inferred λ is close

[12] The electron density of the nebular phase is estimated from the [S II] doublet to be $\sim$few $\times$ 10^2 cm^{-3}. We assume a lower value for ρ_H because the ambient medium density is 4 $\times$ smaller than the shocked density in a nonradiative shock.

to the ratio $\rho_{\rm mid}/\rho_{\rm diffuse} \sim 300$. Thus, our analytic model is self-consistent and has the potential to be applied quantitatively to realistic observations of AGN-jet-driven cocoons.

The other noteworthy feature of J1316+1753 is that the cocoon (traced by [O III] emission) is symmetric relative to the galactic center rather than around the jet hot spots offset by $\approx$1.5 kpc from the center. This suggests that the galaxy's minor axis provides the path of least resistance (with the lowest column density) for the cocoon to move. A low-density CGM along the galaxy minor axis is indeed seen in cosmological simulations (e.g., Nelson et al. 2019; Yang et al. 2024)[13] and inferred from observations (Martín-Navarro et al. 2021; Zhang & Zaritsky 2022). This implies that Fermi/eROSITA bubbles (FEBs) in the center of the Milky Way (MW), which display left–right and up–down symmetry, may be produced by inclined jets that dissipate within $\lesssim$1 kpc from the center as in J1316+1753 (see Sarkar et al. 2023 and Section 5.5 for further discussion).

5.2.3. Realistic Clumpy Medium

To minimize the number of parameters needed to describe the clumpy medium, we assume that the ISM has uniformly randomly distributed spherical clouds with a specified density contrast, volume filling fraction, and cloud size. However, the ideas presented for our simple cloudy ISM are generically applicable. Namely, the jet interacts strongly with the clouds on its path, and the clouds away from the jet beam are slowly engulfed by the hot cocoon without as much interaction.

A more realistic distribution is a multiphase ISM+CGM with a distribution across a range of densities. Suppose that the volume probability density function (pdf) overdensity has separate peaks (e.g., $t = 0$ pdf in Figure 2 of Mukherjee et al. 2016, and even at later times). In that case, we can still calculate the effective density encountered by the jet as given by Equation (23), with ρ_H as the density peak value of the phase with largest f_V, $\rho_{\rm cl}$ as the density peak value of the dense phase, and $f_L \approx 0.6 f_V^{1/3}$ (Equation (31)), where f_V is the volume fraction of the dense phase. For Mukherjee et al. (2016), then, $\rho_H \approx 0.1\,{\rm cm}^{-3}$ and $\rho_{\rm cl} \approx 100\,{\rm cm}^{-3}$, and $f_V \approx 0.045$ (mentioned in (III) of their Section 3) gives $f_L \approx 0.21$. Thus, our Equation (23) gives $\lambda \approx 55$, which, according to Equation (27), is well within the dissipated regime. Indeed, the jet head in the second row of Figure 5 (time = 0.56 Myr) of Mukherjee et al. (2016) is dissipated within a spherical cocoon. Later, when the jet head exits the ISM and enters the nonclumpy CGM, the cocoon becomes anisotropic, and the jet is not dissipated.

While a multipeaked volume pdf appears to be a decent approximation for a two-phase medium that we consider, the volume pdf can be more general. However, our idea that the jet encounters a higher effective density than the cocoon still applies. In this case, the effective density parameter λ may be given by

$$\lambda \sim \frac{\langle \sqrt{\rho} \rangle_L^2}{\rho_H}, \tag{35}$$

where $\langle\rangle_L$ represents the average over the length pdf (related to the volume pdf; recall from Section 3.3.3 that the length covered by clouds rather than their volume fraction matters for effective density encountered by the jet) and ρ_H is the density corresponding to the global maximum of the volume pdf.

5.2.4. Magnetic Fields and Plasma Transport

We model the jets hydrodynamically, but the jets are expected to be magnetically dominated. A large-enough magnetic field dominated by the azimuthal component can become unstable to the kink instability (e.g., Tchekhovskoy & Bromberg 2016; Mukherjee et al. 2020), which can dissipate the jet internally rather than as a result of interaction with the clumps. Quantifying the relative role of magnetic instabilities and clumpiness in dissipating the AGN jet will be useful, but this investigation is left for the future. We have also not modeled the synchrotron emission from such magnetized jets (see Hardcastle & Krause 2014 as an example of a work that calculates jet+cocoon emission). For simplicity, we also do not include plasma transport processes such as thermal conduction and viscosity.

5.2.5. Relativistic Effects

Since in our model the outer cocoon properties (v_h, v_c, and P_c) are found to be independent of the jet velocity v_j, we can expect the relations for these to be close approximations even for mildly relativistic jets. However, for highly relativistic jets ($\Gamma \gg 1$), the prefactors would be different, as calculated analytically in Bromberg et al. (2011). For such jets in a uniform or smoothly stratified medium, the calibrated models presented in Harrison et al. (2018) would be more appropriate. For simulations of hydrodynamic and MHD relativistic jets, see English et al. (2016). We also exclude the effect of cosmic rays, which could contribute to the internal energy of the jet/cocoon and modify the dynamics.

5.3. Jet–ISM Interaction Time and AGN Feedback

As long as the jet is active, the jet head can drill through a dense, cloudy medium. However, after the jet is off (called choked jet in Sarkar et al. 2023; see also Yang et al. 2022), the shocked ISM crushes the inner cocoon, and shock+bubble evolution is governed by the ambient density gradient and buoyancy. For a sufficiently energetic jet event, most energy is deposited in the CGM (not the ISM) via shocks and mixing. Some of the heating can also go into cosmic rays, dissipation of sound waves, or turbulence (reviewed by Bourne & Yang 2023 in the context of the ICM).

If the jet switches off before the cocoon breaks out into the CGM, most of the feedback energy is deposited in the dense ISM (absent in massive elliptical galaxies) and may be radiated away without much long-term self-regulation of star formation. In this case, localized positive feedback in the densest regions is likely, depending on factors such as jet power and orientation and the nature of turbulence in the ISM (Federrath & Klessen 2012; Mukherjee et al. 2018). A few eddy turnover times after the jet switches off and turbulence decays, the molecular gas can cool and form stars prodigiously. More molecular gas can condense from colliding warm clouds (e.g., Heitsch et al. 2006). Thus, the CGM seems to be where jet energy must be deposited for negative feedback to dominate on average (see, e.g., Figure 6 in Fielding et al. 2018, which shows an increase in mechanical efficiency once the superbubble breaks out of the ISM into the CGM; see also Figure 3 in Shchekinov 2018).

[13] In these works, AGN feedback is injected in very different ways, but the propagation of a cocoon preferentially along the galaxy minor axis is a generic outcome.

Let the effective path length that the jet head traverses within the ISM be $l_{\rm ISM}$, and let the time for which the jet is confined inside the ISM of the host galaxy (or the jet–ISM interaction time) be $t_{\rm ISM}$. Then,

$$l_{\rm ISM} = \int v_h \, dt, \tag{36}$$

or

$$l_{\rm ISM} = \frac{10}{3(4\pi)^{1/5}}(1 - f_V)^{-1/5} \times (\theta_0\sqrt{\lambda})^{-4/5}\left(\frac{L_j}{\rho_H}\right)^{1/5} {t_{\rm ISM}}^{3/5}, \tag{37}$$

assuming the jet to be in the nondissipated regime (see Section 3.3.1; Equation (19a)). Now, assuming a constant disk thickness $2H$ and the inclination angle of the jet with respect to the disk normal to be θ_j, we obtain $l_{\rm ISM} = H/\cos\theta_j$. Thus, our model gives the following prediction for the jet–ISM interaction time:

$$t_{\rm ISM} = \left(\frac{3}{10}\right)^{5/3}(4\pi(1 - f_V))^{1/3} \times (\theta_0\sqrt{\lambda})^{4/3}\left(\frac{\rho_H}{L_j}\right)^{1/3}\left(\frac{H}{\cos\theta_j}\right)^{5/3}. \tag{38}$$

The physical significance of $t_{\rm ISM}$ is that it sets the typical time for which the jet interacts directly with the host ISM before it drills through this clumpy ISM. Substituting typical values for the relevant quantities, we obtain

$$t_{\rm ISM} = 0.026\ {\rm Myr}\ (1 - f_V)^{1/3} \times \left(\frac{\theta_{0,10}^4}{L_{j,42}}\right)^{1/3}(\rho_{H,m_p}\lambda^2)^{1/3}\left(\frac{H_{200}}{\cos\theta_j}\right)^{5/3}, \tag{39}$$

where H_{200} is the height of the clumpy medium, in units of 200 pc. Here we have used the numerical calibration of z_h from Figure 3.

This shows, for instance, that nearly dissipated jets facing $\lambda \approx 100$ can be confined within the ISM for a time $\gtrsim$5 Myr, provided that they are low-power ($L_j \lesssim 10^{41}\,{\rm erg\,s^{-1}}$) jets launched with a sufficiently large ($\gtrsim$65°) angle of inclination with respect to the disk normal. This time increases if jets with lower power or wider opening angles are considered. The jet duty cycle (fraction of the time that the jet is ON) is important for jet–ISM interaction, but the duration of individual jet events is even more important. Longer ON states of the radio jet make it easier for the jet to deposit its energy in the less radiative CGM rather than being stopped in the radiative ISM.

5.4. Anisotropy of Jet Power and AGN Feedback in Simulations

Cosmological simulations are typically large-volume ($\approx$[100 Mpc]^3) or zoom simulations of a single dark matter halo, evolved over $\gtrsim$1 Gyr to study the formation and evolution of galaxies (Vogelsberger et al. 2020). The spatial resolution in cosmological simulations is $\gtrsim$100 pc (see, e.g., Table 2 of Vogelsberger et al. 2020), much larger than the jet radius for typical parameters (Equation (13)). Thus, such simulations cannot evolve self-consistent jets confined by the cocoon pressure for jets with power $\lesssim 10^{42}\,{\rm erg\,s^{-1}}$. The AGN jet implementations in cosmological simulations should be considered effective models injecting enough energy in the CGM to prevent runaway cooling flows. However, the cocoon structure and microphysics of energy dissipation are unresolved.

Since the ratio of the cocoon radius and the jet head is $\sim\theta_0 \ll 1$ (see Equation (25)), the energy injection due to AGN jets should be anisotropic, with the energy propagating primarily in the jet direction. This is accomplished by injecting AGN jets with a specified mass, momentum, and energy flux in the radial direction but confined to a narrow angle $\sim\theta_0$ (e.g., as done in Li et al. 2015; Prasad et al. 2015; Yang & Reynolds 2016). In fact, a range of feedback prescriptions, as long as they deposit energy anisotropically (or become effective anisotropic because of the ISM; e.g., Sijacki et al. 2007; Zubovas & Nayakshin 2012; Gabor & Bournaud 2014; Cielo et al. 2018; Nelson et al. 2019), can produce galaxy and CGM properties in broad agreement with observations (provided that the events are energetic enough to escape the dense central region). In the context of the ICM, if AGN energy is deposited isotropically, the jets do not propagate far from the cluster core but are smothered by excessive cooling in the dense cluster core with a short cooling time (Meece et al. 2017). Jet energy can be deposited at large radii by anisotropic jets, preventing excessive cooling over cosmological timescales. Only anisotropic jets allow energy to be transported to large radii and control long-term cooling flows, even though cooling episodes lead to short starbursts.

Our analytic model provides a framework for injecting isotropic or jetted AGN feedback depending on the clumpiness assumed at scales below the numerical resolution. Equations (24), (23), and (27) give the threshold for clumpiness (λ) beyond which the cocoon is expected to be isotropic, and physically consistent feedback should be isotropic. With smaller clumpiness, energy, and mass can be injected over a narrower angle $\sim\theta_0$, corresponding to a cocoon launched by a narrow jet in a uniform medium. We can make the subgrid energy injection prescriptions more sophisticated by smoothly interpolating the anisotropy of injection of AGN power between the uniform and the fully dissipated regime, depending on the clumpiness of the ISM as quantified by λ.

5.5. Fermi/eROSITA Bubbles

The origin of the FEBs has been discussed in the context of supernova-driven wind or AGN activity from Sgr A* (Su et al. 2010; Zubovas & Nayakshin 2012; Crocker et al. 2015; Mou et al. 2015; Sarkar et al. 2015, 2017; Sarkar 2019; Mondal et al. 2022; Yang et al. 2022; Zhang & Zaritsky 2022). See Sarkar (2024) for a detailed review of the topic. While the supernova-driven wind naturally follows the density gradient of the galaxy and produces symmetric FEBs, the AGN-jet-driven events are not expected to follow the density gradient unless the jet is dissipated within the ISM. It was argued by Sarkar et al. (2023) that any past activity Sgr A* jet was most probably inclined relative to the Galaxy rotation axis, and any such inclined jets would produce asymmetric FEBs, unlike the observed ones. Therefore, a successful jet-driven FEB model requires the jet to be dissipated. However, such a choked jet would produce a stronger shock than the observations and is ruled out as a possible explanation for the FEBs.

The current paper provides a framework to check whether any past jets in the MW could have been dissipated. The MW ISM is characterized by a typical volume filling density of $\rho_H \sim 1 m_p$ cm^{-3}, in which more dense gas such as diffuse H_2 phase ($\rho_{\rm cl} \sim 100 m_p$ cm^{-3}, $f_V \sim 10^{-3}$) or dense H_2 phase ($\rho_{\rm cl} \sim 10^4 m_p$ cm^{-3}, $f_V \sim 10^{-4}$) resides (Draine 2011). Now, combining Equation (23) and that $f_L \approx 0.6 f_V^{1/3}$ (from Figure 8), we estimate that the MW ISM can be described by $\lambda \sim 2.4$ and $\lambda \sim 14$ for the diffuse H_2 and dense H_2 phases, respectively. A comparison to Equation (27) shows that in the MW ISM, $\lambda < \lambda_{\rm crit}$. This means that the MW ISM is not expected to dissipate any jets from Sgr A* strongly, and jets should blow asymmetric bubbles relative to the MW's minor axis.

One possibility, however, remains. It is the interaction of the jet with the Central Molecular Zone (CMZ). The CMZ is an elliptical ring (semimajor axis $\approx$ 100 pc) of dense molecular gas around the Galactic center (Molinari et al. 2011). The dense gas in the CMZ has a density of $\sim 10^3 m_p$ cm^{-3} (Morris & Serabyn 1996; Molinari et al. 2011; Henshaw et al. 2016) and lies on the Galactic plane. Given that the "best-bet" rotation axis of the central SMBH lies close to the disk (Event Horizon Telescope Collaboration et al. 2022), it could well be possible that the past jet had interacted with the CMZ. Now, considering that the CMZ ring has an inner and outer radius of 60 and 100 pc, respectively, and that its height is $\sim$20 pc, the volume filling factor for the CMZ within the ISM scale height is $\sim$0.06 (assuming an ISM scale height of 200 pc). This implies that the CMZ has $\lambda \sim 70 \gg \lambda_{\rm crit}$. Therefore, it is plausible that if the MW jet interacts with the CMZ, it could be dissipated to produce the symmetric FEBs. Such an interaction would, however, be imprinted on the structure of the CMZ as breaks in dense gaseous rings. A detailed study of such a scenario remains for future work.

5.6. Ubiquity of Low-power Jets in Massive Galaxies

The earliest detected radio jets and bubbles were naturally very powerful, but the most common radio jets appear to be compact and lower in power, not only in elliptical galaxies and clusters but also in disk galaxies (e.g., Baldi et al. 2018; Sabater et al. 2019). Moreover, luminous radio jets ($L_{150\,\rm MHz} \gtrsim 10^{23}$ W Hz^{-1}, or $L_{\rm jet} \gtrsim 10^{43}$ erg s^{-1}) are exceedingly rare in star-forming galaxies but are almost exclusively found in massive elliptical galaxies (see Figure 4 in Sabater et al. 2019). Most importantly, galaxies with stellar mass $\gtrsim 10^{11} M_\odot$ almost always have $L_{150\,\rm MHz} \gtrsim 10^{21}$ W Hz^{-1} or $L_{\rm jet} \gtrsim 2 \times 10^{41}$ erg s^{-1}. A higher jet power in more massive galaxies/halos implies a tight feedback coupling between the cooling of the CGM/ICM and accretion power in massive halos.

Recent observations have shown that most radio sources in the local universe are compact jets with linear sizes $\lesssim$5 kpc, in contrast to the extended radio emission from FR I− and FR II −type jets. These have been termed as FR 0 jets (Baldi et al. 2018). As discussed in Baldi et al. (2018), these sources are more numerous than expected if these are simply young FR I jets. On the other hand, their galactic environment seems similar to that of FR I jets—both are hosted by elliptical galaxies. This suggests that they are intrinsically different, possibly having lower power or shorter active lifetimes than FR I jets. These observations imply that such FR 0 jets will likely spend a significant fraction of the active lifetime within the host galaxy. As a result, the jet's interaction with the dense gas in the core would significantly affect the jet+cocoon dynamics and the resulting feedback on the galaxy.

Elliptical galaxies typically lack a dense ISM, and the jets propagate in the hot ICM/CGM. The CGM pressure/temperature scales with the halo mass as $\propto M_{\rm halo}^{2/3}$, but the CGM density within $\lesssim$10 kpc is similar (see, e.g., Figure 2 in Sharma et al. 2012). A cocoon propagating in the hot CGM will eventually reach pressure equilibrium with the CGM and then evolve buoyantly. Using Equations (11a)–(11c), the cocoon radius when it reaches the ambient pressure P_a is

$$R_{c,\rm buoy} \approx 1.6\ {\rm kpc} \left(\frac{\theta_{0,10}^2 L_{j,42}^2 \rho_{H,m_p}}{P_{a,-10}^3} \right)^{1/4}, \quad (40)$$

where the ambient pressure is normalized to 10^{-10} dyn cm^{-2}, comparable to the ICM temperature of 10^7 K and number density of 0.1 cm^{-3}.[14] Note that this estimate is only weakly dependent on the density profile for any reasonable model of the ICM (see Appendix B.1 of Bromberg et al. 2011). The corresponding head location is $z_h \approx 7.4$ kpc (using Equation (25)). This implies that the mechanical power of FR 0 jets with size $\lesssim$5 kpc is $\lesssim 10^{42}$ erg s^{-1}. This limit corresponds to $L_{1.5\,\rm GHz} \approx 2.5 \times 10^{21}$ W Hz^{-1} (see the equation relating cavity power to radio power in Sabater et al. 2019). Reading off from Figure 5 (right panel) in Sabater et al. (2019), $\gtrsim$85% of galaxies with $M_\star \lesssim 10^{11} M_\odot$ have radio luminosity smaller than this value, thus making FR 0 galaxies the most numerous radio jets in the local Universe, quantitatively consistent with Baldi et al. (2018).

While the number of galaxies is dominated by the lowest radio power FR 0 jets, the total jet power is dominated by the galaxies at the cutoff jet/cavity radio power, which for star-forming galaxies is $L_{1.5\,\rm GHz} \sim 10^{22}$ W Hz^{-1} and for the AGN sample is $\sim 10^{25}$ W Hz^{-1} (see, e.g., Figure 4 in Sabater et al. 2019), corresponding to $P_j \sim 10^{42}$ and 10^{44} erg s^{-1}, respectively.

6. Summary

Here is a very brief summary of our paper:

1. We extend the analytic model of a self-collimated hydrodynamical conical jet injected into a uniform medium to a clumpy medium characterized by the density ratio of the cold clouds relative to the diffuse medium $\rho_{\rm cl}/\rho_H$, the volume filling fraction f_V, and the cloud radius $R_{\rm cl}$. We calibrate the cocoon radius and the jet head height with numerical simulations (see Figure 3). The ratio of the cocoon radius to the jet head location depends only on the jet injection angle θ_0 (Equation (25)). The key physical insight behind our model is that the supersonic jet encounters a much higher effective density (given by Equation (23)) compared to the subsonic cocoon that effectively encounters the diffuse medium. The ratio of the effective density encountered by the jet and the cocoon λ depends on the density contrast between clouds and the diffuse medium ($\rho_{\rm cl}/\rho_H$) and the length fraction in clouds along the jet beam f_L. Our numerical calibration shows that $f_L \approx 0.6 f_V^{1/3}$ for the

[14] Plugging in the typical CGM parameters for the MW, $\rho_{H,m_p} \sim 0.01$ and $P_{a,-10} \sim 0.01$, $R_{c,\rm buoy} \sim 16$ kpc, of order the size of FEBs.

range of cloud sizes we explored. Using the analytic model and calibration with numerical simulations, we find the criterion for strong jet dissipation (Equation (27); see also Section 5.1) as a function of λ and θ_0. Jet dissipation corresponds to the jet being stopped by the clouds along the jet beam well inside the cocoon.

2. Numerical simulations suggest two qualitatively different regimes for the interaction of an AGN jet with the ambient medium: (i) anisotropic regime, in which the jet head moves farther than the cocoon and the cocoon is elongated along the jet; and (ii) dissipated regime, in which the head velocity is smaller than that of the cocoon and the cocoon is isotropic. The dissipated jet regime occurs for sufficiently dense clumps and a large-enough volume filling fraction, the threshold being quantitatively given by $\lambda \gtrsim 20$, where λ is given by Equation (32). These two regimes (see Section 5.4) suggest a simple subgrid model (anisotropic vs. isotropic energy injection) for the implementation of mechanical AGN feedback in galaxy formation simulations. We apply our calibrated analytic models to various astrophysical systems from FEBs to Seyfert/quasar and FR 0 jets in Section 5.

Overall, we present a theoretical framework, for the first time, to describe the dissipation of AGN jets in a clumpy medium and discuss its implications for different modes of jet feedback in galaxies and galaxy clusters. Our models/simulations are still missing some of the key physical processes, such as radiative cooling, magnetic fields, and realistic gravitational and density fields. Strong azimuthal magnetic fields within the jet can make it unstable to magnetic instabilities such as the kink and tearing modes. Similarly, radiative cooling may take away most of the jet energy, and the cocoon expansion can be slowed. We aim to study these important effects in the future.

Acknowledgments

We thank Dipanjan Mukherjee for the helpful discussions. R.D. and P.S. thank Gurkirat Singh and Rajsekhar Mohapatra for their help with getting started with AthenaK. We acknowledge the National Supercomputing Mission (NSM) for providing computing resources for Param Pravega at IISc. K.C.S. is partially supported by the German Science Foundation via DFG/DIP grant STE/ 1869-2 GE/ 625 17-1 in Israel. J.M.S. acknowledges support from the Eric and Wendy Schmidt Fund for Strategic Innovation.

ORCID iDs

Prateek Sharma https://orcid.org/0000-0003-2635-4643
Kartick C. Sarkar https://orcid.org/0000-0002-7767-8472
James M. Stone https://orcid.org/0000-0001-5603-1832

References

Alexander, D., & Hickox, R. 2012, NewAR, 56, 93
Anglés-Alcázar, D., Quataert, E., Hopkins, P. F., et al. 2021, ApJ, 917, 53
Baldi, R. D., Capetti, A., & Massaro, F. 2018, A&A, 609, A1
Bally, J. 2016, ARA&A, 54, 491
Begelman, M. C., & Cioffi, D. F. 1989, ApJL, 345, L21
Begelman, M. C., & Fabian, A. C. 1990, MNRAS, 244, 26
Blandford, R., Meier, D., & Readhead, A. 2019, ARA&A, 57, 467
Blandford, R. D., & Rees, M. J. 1974, MNRAS, 169, 395
Bourne, M. A., & Yang, H. Y. K. 2023, Galax, 11, 73
Bromberg, O., Nakar, E., Piran, T., & Sari, R. 2011, ApJ, 740, 100
Choudhury, P. P., & Reynolds, C. S. 2022, MNRAS, 514, 3765
Cielo, S., Bieri, R., Volonteri, M., Wagner, A., & Dubois, Y. 2018, MNRAS, 477, 1336
Crocker, R. M., Bicknell, G. V., Taylor, A. M., & Carretti, E. 2015, ApJ, 808, 107
de Gouveia Dal Pino, E. M. 1999, ApJ, 526, 862
Draine, B. T. 2011, Physics of the Interstellar and Intergalactic Medium (Princeton, NJ: Princeton Univ. Press)
English, W., Hardcastle, M., & Krause, M. 2016, MNRAS, 461, 2025
Event Horizon Telescope Collaboration, Akiyama, K., Alberdi, A., et al. 2022, ApJL, 930, L16
Fabian, A. C. 2012, ARA&A, 50, 455
Fanaroff, B. L., & Riley, J. M. 1974, MNRAS, 167, 31P
Federrath, C., & Klessen, R. 2012, ApJ, 761, 156
Fielding, D., Quataert, E., & Martizzi, D. 2018, MNRAS, 481, 3325
Forbes, J. C., & Lin, D. N. C. 2019, AJ, 158, 124
Gabor, J., & Bournaud, F. 2014, MNRAS, 441, 1615
Gaibler, V., Khochfar, S., Krause, M., & Silk, J. 2012, MNRAS, 425, 438
Girdhar, A., Harrison, C. M., Mainieri, V., et al. 2022, MNRAS, 512, 1608
Goldsmith, K. J. A., & Pittard, J. M. 2018, MNRAS, 476, 2209
Guo, F. 2015, ApJ, 803, 48
Hardcastle, M., & Krause, M. 2013, MNRAS, 430, 174
Hardcastle, M., & Krause, M. 2014, MNRAS, 443, 1482
Hardcastle, M. J., & Croston, J. H. 2020, NewAR, 88, 101539
Harrison, R., Gottlieb, O., & Nakar, E. 2018, MNRAS, 477, 2128
Heitsch, F., Slyz, A. D., Devriendt, J. E. G., Hartmann, L. W., & Burkert, A. 2006, ApJ, 648, 1052
Henshaw, J. D., Longmore, S. N., Kruijssen, J. M. D., et al. 2016, MNRAS, 457, 2675
Heywood, I., Rammala, I., Camilo, F., et al. 2022, ApJ, 925, 165
Huško, F., & Lacey, C. 2023, MNRAS, 520, 5090
Kanjilal, V., Dutta, A., & Sharma, P. 2021, MNRAS, 501, 1143
Klein, R. I., McKee, C. F., & Colella, P. 1994, ApJ, 420, 213
Komissarov, S. S., & Falle, S. A. E. G. 1997, MNRAS, 288, 833
Li, Y., Bryan, G. L., Ruszkowski, M., et al. 2015, ApJ, 811, 73
Mandal, A., Mukherjee, D., Federrath, C., et al. 2021, MNRAS, 508, 4738
Martín-Navarro, I., Pillepich, A., Nelson, D., et al. 2021, Natur, 594, 187
Martizzi, D., Quataert, E., Faucher-Giguère, C.-A., & Fielding, D. 2019, MNRAS, 483, 2465
Matzner, C. D. 2003, MNRAS, 345, 575
McKee, C. F., & Ostriker, J. P. 1977, ApJ, 218, 148
McNamara, B. R., & Nulsen, P. E. J. 2007, ARA&A, 45, 117
Meece, G. R., Voit, G. M., & O'Shea, B. W. 2017, ApJ, 841, 133
Mirabel, I. F., & Rodríguez, L. F. 1998, Natur, 392, 673
Molinari, S., Bally, J., Noriega-Crespo, A., et al. 2011, ApJL, 735, L33
Mondal, S., Keshet, U., Sarkar, K. C., & Gurwich, I. 2022, MNRAS, 514, 2581
Morris, M., & Serabyn, E. 1996, ARA&A, 34, 645
Mou, G., Yuan, F., Gan, Z., & Sun, M. 2015, ApJ, 811, 37
Mukherjee, D., Bicknell, G. V., Sutherland, R., & Wagner, A. 2016, MNRAS, 461, 967
Mukherjee, D., Bicknell, G. V., Wagner, A. Y., Sutherland, R. S., & Silk, J. 2018, MNRAS, 479, 5544
Mukherjee, D., Bodo, G., Mignone, A., Rossi, P., & Vaidya, B. 2020, MNRAS, 499, 681
Nelson, D., Pillepich, A., Springel, V., et al. 2019, MNRAS, 490, 3234
Oey, M. S. 2009, in AIP Conf. Ser. 1156, The Local Bubble and Beyond II, ed. R. K. Smith, S. L. Snowden, & K. D. Kuntz (Melville, NY: AIP), 295
Prasad, D., Sharma, P., & Babul, A. 2015, ApJ, 811, 108
Raga, A. C., & Canto, J. 1996, MNRAS, 280, 567
Ranjan, D., Oakley, J., & Bonazza, R. 2011, AnRFM, 43, 117
Sabater, J., Best, P. N., Hardcastle, M. J., et al. 2019, A&A, 622, A17
Saikia, D. J. 2022, JApA, 43, 97
Sarkar, K. C. 2019, MNRAS, 482, 4813
Sarkar, K. C. 2024, A&ARv, 32, 1
Sarkar, K. C., Mondal, S., Sharma, P., & Piran, T. 2023, ApJ, 951, 36
Sarkar, K. C., Nath, B. B., & Sharma, P. 2015, MNRAS, 453, 3827
Sarkar, K. C., Nath, B. B., & Sharma, P. 2017, MNRAS, 467, 3544
Scheuer, P. A. G. 1974, MNRAS, 166, 513
Sharma, P., McCourt, M., Parrish, I. J., & Quataert, E. 2012, MNRAS, 427, 1219
Sharma, P., Roy, A., Nath, B. B., & Shchekinov, Y. 2014, MNRAS, 443, 3463
Shchekinov, Y. 2018, Galax, 6, 62
Sijacki, D., Springel, V., Di Matteo, T., & Hernquist, L. 2007, MNRAS, 380, 877
Stone, J. M., Tomida, K., White, C. J., & Felker, K. G. 2020, ApJS, 249, 4
Su, M., Slatyer, T. R., & Finkbeiner, D. P. 2010, ApJ, 724, 1044

Sutherland, R. S., & Bicknell, G. V. 2007, ApJS, 173, 37
Tanner, R., & Weaver, K. A. 2022, AJ, 163, 134
Tchekhovskoy, A., & Bromberg, O. 2016, MNRAS, 461, L46
Venturi, G., Cresci, G., Marconi, A., et al. 2021, A&A, 648, A17
Vogelsberger, M., Marinacci, F., Torrey, P., & Puchwein, E. 2020, NatRP, 2, 42
Wagner, A., & Bicknell, G. 2011, ApJ, 728, 29
Wagner, A., Bicknell, G., & Umemura, M. 2012, ApJ, 757, 136
Wagner, A., Umemura, M., & Bicknell, G. 2013, ApJL, 763, 18
Wang, Z., Wiita, P. J., & Hooda, J. S. 2000, ApJ, 534, 201
Weaver, R., McCray, R., Castor, J., Shapiro, P., & Moore, R. 1977, ApJ, 218, 377
Weinberger, R., Ehlert, K., Pfrommer, C., Pakmor, R., & Springel, V. 2017, MNRAS, 470, 4530
Weinberger, R., Su, K.-Y., Ehlert, K., et al. 2023, MNRAS, 523, 1104
Yadav, N., Mukherjee, D., Sharma, P., & Nath, B. B. 2017, MNRAS, 465, 1720
Yang, H. Y. K., & Reynolds, C. S. 2016, ApJ, 829, 90
Yang, H. Y. K., Ruszkowski, M., & Zweibel, E. G. 2022, NatAs, 6, 584
Yang, T., Davé, R., Cui, W., et al. 2024, MNRAS, 527, 1612
Yates-Jones, P., Shabala, S., & Krause, M. 2021, MNRAS, 508, 5239
Zhang, H., & Zaritsky, D. 2022, ApJ, 941, 18
Zubovas, K., & Nayakshin, S. 2012, MNRAS, 424, 666
Zubovas, K., Sabulis, K., & Naujalis, R. 2014, MNRAS, 442, 2837